International Journal of Heat and Mass Transfer 119 (2018) 372–391

Contents lists available at ScienceDirect

International Journal of Heat and Mass Transfer

journal homepage: www.elsevier.com/locate/ijhmt

Two-dimensional analytical investigation of coupled heat and mass transfer and entropy generation in a porous, catalytic microreactor

Graeme Hunt [a], Nader Karimi [a,*], Mohsen Torabi [b]

[a] School of Engineering, University of Glasgow, Glasgow G12 8QQ, United Kingdom
[b] The George W. Woodruff School of Mechanical Engineering, Georgia Institute of Technology, Atlanta, GA 30332, USA

ARTICLE INFO

Article history:
Received 7 July 2017
Received in revised form 3 November 2017
Accepted 21 November 2017

Keywords:
Microreactors
Porous media
Entropy generation
Advective-diffusive transport
Soret effect
Analytical modelling

ABSTRACT

Influences of the solid body of microreactors (or the microstructure) upon the transfer processes and hence on the performance of microreactors have been recently emphasised. Nonetheless, the subtle connections between microstructure design and micro-transport phenomena are still largely unknown. To resolve this, the current paper presents an analytical study of the advective-diffusive transport phenomena in a microreactor filled with porous media and with catalytic surfaces. The system under investigation includes the fluid and porous solid phases inside a microchannel with thick walls and subject to uneven thermal loads. The thermal diffusion of mass, viscous dissipation of the flow momentum and local thermal non-equilibrium in the porous medium are considered. The axial variations of heat and mass transfer processes are also taken into account and two-dimensional solutions of the temperature and concentration fields are provided. The local and total entropy generation within the system are further calculated. The results clearly demonstrate the major influences of thick walls on the thermal behaviour and subsequently on the mass transfer and entropy generation of the microreactor. In particular, the Nusselt number is shown to be strongly dependent upon the configuration of microstructure such that it decreases significantly by thickening the walls. The results also demonstrate that for finite Soret numbers the total irreversibility of the system is dominated by the Soret effect. The analytical results of this work can be further used for the validation of future numerical analyses of microreactors.

1. Introduction

Microreactors continue to grow in significance in various technological areas [1,2]. Broadly, these include process intensification in chemical industry [3,4], while specialised applications such as distributed fuel production [5–7] and nanoparticle generation [8] are also under development. Further, over the last two decades, there have been sustained attempts for developing microcombustors for the purpose of micro power generation [9]. In general, microreactors have been identified as being most suitable for catalytic and highly exothermic and endothermic reactions [5,10]. This is essentially because of the fact that transport phenomena are highly enhanced in microreactors and hence thermal energy can be readily added to or removed from these systems [3,11]. Compared to macro-reactors, microreactors feature much smaller characteristic lengths and thus they are far more efficient in diffusion of heat and mass in laminar regimes [3]. Nonetheless, recent investigations indicate that optimisations of transport characteristics and second law performance of these devices are rather involved [12–14]. This is mainly due to the strong coupling of transport of heat with the microstructure of the reactor that primarily includes the surrounding walls [12,14]. In most cases, the thermal characteristics affect mass transfer and entropy generation, which are central to the optimal design and performance of the system.

Temperature fields and heat transfer in microreactors have been already examined experimentally, e.g. Refs. [15,16]. Nevertheless, the small size of microreactors makes them a challenging medium for experimental measurements and equally amenable to numerical and theoretical investigations [12,17]. Most existing modelling works in this area emphasise the influences of heat and mass transfer upon the overall operation of the reactor. In their review of thermo-hydraulics of microreactor clusters, Rebrov et al. [18] highlighted the significance of microstructure on the heat transfer behaviour of the system. They showed that heat transfer in the clusters of microreactors is heavily dependent on the materials and configurational specifications of the system [18]. Yet, the focus of their survey was on the bundles of individual microreactors and therefore they did not consider the details of heat transfer in a single reactor [18].

* Corresponding author.
E-mail address: Nader.Karimi@glasgow.ac.uk (N. Karimi).

https://doi.org/10.1016/j.ijheatmasstransfer.2017.11.118
0017-9310/

Nomenclature

a_{sf}	interfacial area per unit volume of porous media
Bi	Biot number
Br'	modified Brinkman number
C	mass species concentration
C_0	inlet concentration
C_p	specific heat capacity
D	effective mass diffusion coefficient
Da	Darcy number
D_T	coefficient of thermal mass diffusion
h_1	half-thickness of the microchannel
h_2	half-height of microchannel
h_{sf}	interstitial heat transfer coefficient
H_w	wall heat transfer coefficient
k	effective thermal conductivity ratio of the nanofluid and the porous solid
k_1	thermal conductivity of wall 1
k_2	thermal conductivity of wall 2
k_{e1}	ratio of thermal conductivity of wall 1 and thermal conductivity of the porous solid
k_{e2}	ratio of thermal conductivity of wall 2 and thermal conductivity of the porous solid
k_{enf}	effective thermal conductivity of the nanofluid phase
k_{es}	effective thermal conductivity of the solid phase of the porous medium
k_R	reaction rate constant on the walls
L	length of the microchannel
M	viscosity ratio
N_{DI}	dimensionless diffusive irreversibility
N_{FF}	dimensionless fluid friction irreversibility
N_{int}	dimensionless interstitial heat transfer irreversibility
N_{nf}	dimensionless nanofluid and interstitial irreversibility
$N_{nf,ht}$	dimensionless nanofluid heat transfer irreversibility
N_s	dimensionless porous solid and interstitial irreversibility
$N_{s,ht}$	dimensionless heat transfer irreversibility
N_{w1}	dimensionless lower wall irreversibility
N_{w2}	dimensionless upper wall irreversibility
N_{pm}	dimensionless total porous medium irreversibility
N_{Tot}	dimensionless total entropy
Nu	Nusselt number
p	pressure
Pe	Peclet number
X	dimensionless axial coordinate
Pr	Prandtl number
Q	wall heat flux ratio
q_1''	lower wall heat flux
q_2''	upper wall heat flux
Re	Reynolds number
R	specific gas constant
S	shape factor of the porous medium
$\dot{S}_{Di}'''$	volumetric entropy generation due to mass diffusion
$\dot{S}_{FF}'''$	volumetric entropy generation due to fluid friction
$\dot{S}_{nf}'''$	volumetric entropy generation in the nanofluid
$\dot{S}_s'''$	volumetric entropy generation in the porous solid
$\dot{S}_{w2}'''$	volumetric entropy generation rate from lower wall
Sr	Soret number
T	temperature
u	nanofluid velocity
$\bar{u}$	average velocity over cross-section
Y	dimensionless transverse coordinate
x	dimensional axial coordinate
y	dimensional transverse coordinate

Greek symbols

μ	dynamic viscosity
κ	permeability
ρ	density
θ	dimensionless temperature
Φ	dimensionless concentration
ξ	aspect ratio of the microchannel
ε	porosity of the porous medium
γ	Damköhler number
ω	dimensionless heat flux defined in Eq. (40)
φ	irreversibility distribution ratio defined in Eq. (41)

Subscripts

$w1$	of the lower wall surface
$w2$	of the upper wall surface
f	base fluid
P	nanoparticles
s	of porous solid
nf	of nanofluid
1	of lower wall
2	of upper wall

In a series of numerical works, Chein and co-workers investigated the behaviour of catalytic microreactors used for fuel reforming [19–22]. Through assuming local thermal equilibrium (LTE) and Fickian mass transfer, the temperature and species fields, Nusselt number and chemical conversion rates and chemical efficiencies were computed in a micro-reformer with porous catalytic layers [19]. It was concluded that the reactor performance is dominated by the configuration of the porous catalyst [19]. This numerical work was later extended to the analyses of the effects of thermal resistance upon steam reforming of methanol in microreactors [20,21]. Chein et al. [20,21] showed that to optimise the reactor it is essential to carefully minimise the thermal resistances within the system. In a separate work, Chein et al. investigated the influences of microstructure configuration and materials on the conversion rates of a micro-reformer and made a number of design suggestions [22]. These findings clearly demonstrate the significance of accurate prediction of heat transfer rates in the design of microreactors. Importantly, almost all existing studies on transport phenomena in porous microreactors assumed LTE in the porous region [19–22]. However, recent studies on porous channels with exothermic or endothermic processes assert that an accurate prediction of the thermal behaviour of such systems warrants a local thermal non-equilibrium (LTNE) analysis [23–26]. In particular, the most recent theoretical studies of microreactors have confirmed that taking LTNE approaches are essential for the accurate prediction of the thermal and entropic behaviours of these systems [12,13].

Most microreactors consist of microchannels and therefore share their heat transfer characteristics with them. Early analyses of porous microchannels included LTE assumption e.g. [27] and LTNE investigation of microchannels have been only reported in recent years. Buonomo et al. [28] conducted an analytical LTNE study of forced convection in a porous microchannel with a rarefied gas flow. These authors [28] showed that heat transfer increases as Biot number increases and reaches asymptotic values. Through considering the viscous forces in porous microchannels,

Ting et al. [29] conducted an LTNE analysis on a nanofluid filled porous microchannel. This study clearly revealed that neglecting viscous dissipations in porous microchannels could result in significant overestimation of the Nusselt number [29]. The effects of nanofluid viscous dissipations upon heat transfer were also investigated in clear microchannels [30,31] and porous microchannels with internal heat generation within the solid phase [32]. These investigations showed that the inclusion of viscous dissipations is a necessity for the precise prediction of thermal processes in microchannels with liquid and nanofluid flow. The studies of Buonomo et al. [28] and Ting et al. [29–32] neglected the finite thickness of the channel wall. Although such assumption is widely made in the analysis of macro-channels, the validity of neglecting wall thickness in microchannels is less obvious. This is due to the fact that, in microchannels the channel height or diameter is very comparable to the thickness of the wall. Existing analyses in clear microchannels [33] and recent studies on porous microchannels [12,13,34,35] have rigorously demonstrated the significant influences of thick walls upon the heat transfer in these systems. Nonetheless, inclusion of wall effects on porous microchannels with strong axial advection has, thus far, remained unexplored.

The analysis of mass transfer in microreactors usually involves solution of a diffusion-advection equations on the basis of a simple Fickian mass diffusion [36–38]. Microreactors have been identified as suitable for coupled heat and mass transfer processes due to Soret effect [3], which is of importance in catalytic reactions [39]. However, so far, Soret effect has received very limited attention in microreactor and microchannel investigations. Habib-Matin and Pop investigated heat and mass transfer in a porous microchannel with catalytic internal surfaces [40]. These authors considered a simple one-dimensional diffusion of mass through a concentration diffusion mechanism as well as a thermodiffusion (Soret) effect. They derived analytical solutions for the LTE temperature and concentration fields in an axisymmetric configuration with zero wall thickness [40]. The general problem of thermodiffusion in porous media has been analysed in a relatively small number of investigations, e.g. [41–43]. However, analysis of thermodiffusion effects under LTNE and for more realistic thick wall microreactors is yet to be conducted.

Similar to that in macro-reactors, entropy generation in microreactors is of high significance [3]. Surprisingly, however, the existing works on entropy generation in microreactors are almost entirely limited to micro-combustors, see for example Refs. [44–46]. Notably, currently there is nearly no work on the entropic behaviours of porous micro-reactors. Exceptions to this, are the most recent works of Elliot et al. [13] and Torabi et al. [14], who investigated heat and mass transfer and entropy generation in a catalytic microreactor. Nonetheless, these analyses were one-dimensional and hence had limited applications. Thus, the existence of a gap in the studies of entropy generation in microreactors is evident. This shortcoming requires immediate attention as it is now well-demonstrated that microreactors are sophisticated thermochemical systems, which can feature non-straightforward entropic behaviours [20,21,37]. Further, recent investigations on porous microchannels have clearly shown the richness of the problem of entropy generation in these systems. As such, Ting et al. [32,47] theoretically examined entropy generation in microchannels with inserted nanofluid-filled porous media. They took an LTNE approach and conducted a two-dimensional, analytical solutions for the temperature fields and local entropy generation [32,47]. Their results mapped the influences of different mechanisms of entropy generation in a porous microchannel. In particular, they highlighted the significance of hydrodynamic irreversibilities in cases with viscous convection of nanofluids [32]. Other theoretical works on the convection of nanofluids in heat generating/consuming porous channels demonstrated the necessity of considering LTNE for the accurate prediction of irreversibilities [26,48]. Another important factor complicating the irreversibilities of microreactors is the influences of solid thick walls. Recent studies on chemically inert microchannels have revealed the strong effects of the thick walls upon the rate of entropy generation [34,49,50]. This is essentially due to the effects of the solid thick walls upon the thermal fields in the microchannel, which in turn influences the rates of entropy generation [49]. Yet, the entropic influences of the thick walls on thermo-diffusive systems have just started to receive attention [14] and remain far from being well understood.

The preceding survey of literature reveals a number of important points about the current state of transport and entropy generation analyses in microreactors. First, with the exception of the most recent work of the authors [12], porous microreactors have not been analysed from an LTNE view even though the importance of such analysis is now well-demonstrated [23–26,35]. Second, there exists a major shortage of studies on the details of internal heat transfer in microreactors. In particular, the three-way interactions amongst the fluid phase, porous solid phase and microstructure of the reactor require further investigations. Third, the subject of thermo-diffusion in microreactors has received very limited attention. This topic is of high relevance to catalytic reactions and hence its inclusion in microreactor analysis is a crucial necessity. Finally, so far, the research on irreversibilities of microreactors has been exclusively focused on non-porous micro-combustors, e.g. [45,46]. Extension of these investigations to porous and particularly porous-catalytic microreactors is yet to be accomplished. Given these, the current study aims to establish a deeper understanding of the transport phenomena and irreversibilities, and their interactions with the microstructure in catalytic microreactors. Such understanding will be vital for the design and optimisation of practical microreactors.

2. Analytical methods

2.1. Problem configuration and assumptions

Fig. 1 illustrates the schematics of the problem under investigation. The microreactor consists of a single microchannel fully filled by porous materials. The system includes a microstructure consisting of two thick walls subject to unequal thermal fluxes and the internal surface of the microchannel is covered by a catalytic coating. A nanofluid flow enters the reactor from the left side. The following assumptions are made through the current analysis.

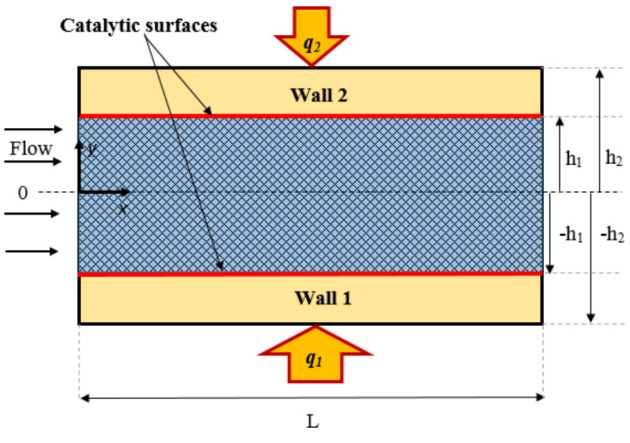

Fig. 1. Schematics of the microreactor under investigation.

- The chemical reactions in the model microreactors shown in Fig. 1 are limited to a zeroth-order reversible, catalytic reaction. Also, in keeping with the previous theoretical analysis of catalytic reactions in microchannels [19,20,40], the catalyst is assumed to be located on the internal surfaces of the channel.
- The effects of temperature variations on the catalytic reaction are ignored [40].
- The porous medium is homogenous, isotropic and fluid saturated and is under LTNE. Further, gravitational effects and radiative heat transfer are ignored.
- The nanofluid flow is steady and laminar satisfying the no-slip boundary conditions on the wall. Further, thermally and hydrodynamically fully developed conditions hold in the entire channel and there exist a no-slip boundary condition on the internal surface of the channel.
- Physical properties such as porosity, specific heat, density, coefficient of thermal diffusion of mass and thermal conductivities are invariants and thermal dispersion is ignored.
- The nanoparticles are uniformly distributed throughout the fluid forming a homogenous phase.
- Processes featuring abrupt reaction zones, separating hot and cold flows, such as those in micro-combustors [44,45] are not considered here. As a result, the axial conduction of heat within the walls is insignificant and is neglected throughout the analysis. This is further justified by noting that experimental studies [1] have already shown that the axial temperature gradient within the microstructure diminishes in thick wall microreactors.

It should be noted that the existence of nanofluid is not central to the current analysis. Nanofluids are considered for the sake of completeness of the study and their practical relevance to the subject of nanoparticle generation in microreactors [8].

2.2. Governing equations and boundary conditions

The Darcy-Brinkman model of transport of momentum governs the hydrodynamics of the system. That is

$$-\frac{\partial p}{\partial x}+\mu_{eff}\frac{\partial^2 u}{\partial y^2}-\frac{\mu_{nf}}{\kappa}u=0 \quad -h_1\leqslant y<h_1 \tag{1}$$

The transport of thermal energy within the solid and fluid phases of the microreactor are governed by the followings [12,32].

$$k_2\frac{\partial}{\partial y}\left[\frac{\partial T_2}{\partial y}\right]=0 \quad h_1<y\leqslant h_2 \tag{2a}$$

$$k_{enf}\frac{\partial^2 T_{nf}}{\partial y^2}+h_{sf}a_{sf}(T_s-T_{nf})+\frac{\mu_{nf}}{\kappa}u^2+\mu_{eff}\left(\frac{\partial u}{\partial y}\right)^2 = \rho_{nf}C_{p,nf}u\frac{\partial T_{nf}}{\partial x} \quad -h_1\leqslant y<h_1 \tag{2b}$$

$$k_{es}\frac{\partial^2 T_s}{\partial y^2}-h_{sf}a_{sf}(T_s-T_{nf})=0 \quad -h_1\leqslant y<h_1 \tag{2c}$$

$$k_1\frac{\partial}{\partial y}\left[\frac{\partial T_1}{\partial y}\right]=0 \quad -h_2\leqslant y<-h_1 \tag{2d}$$

Appendix A shows how the thermophysical properties of nanofluid are calculated from those of the base fluid and nanoparticles. It is emphasised that heat generation by viscous dissipation has been included in Eq. (2b) [32].

Mass transfer of chemical species is governed by the following advective-diffusive model, which takes into account contributions from the Soret effect in addition to the Fickian diffusion of species [51].

$$u\frac{\partial C}{\partial x}=D\frac{\partial^2 C}{\partial y^2}-D_T\frac{\partial^2 T_{nf}}{\partial y^2} \quad -h_1\leqslant y<h_1 \tag{3}$$

The negative sign on the right hand side of Eq. (3) arises from the fact that depending upon the relative size of the diffusive molecules and the base fluid, Soret number can be either positive or negative [51]. Here negative Soret number is presented by a negative sign in front of a positive D_T. It should be noted that the mass diffusion coefficient presented above is the effective mass diffusion coefficient due to the effect of the porous medium in which it operates.

The momentum and heat transport equations are subject to the following boundary conditions [12,32]:

$$y=h_2: \quad k_2\left.\frac{\partial T_2}{\partial y}\right|_{y=h_2}=q_2'' \tag{4a}$$

$$y=h_1:\ u_{nf}=0,\ T_2=T_{nf}=T_s=T_{w2},\ q_2''=k_{enf}\left.\frac{\partial T_{nf}}{\partial y}\right|_{y=h_1}+k_{es}\left.\frac{\partial T_s}{\partial y}\right|_{y=h_1} \tag{4b}$$

$$y=0: \quad \frac{du_{nf}}{dy}=0 \tag{4c}$$

$$y=-h_1: \quad u_{nf}=0, \quad T_1=T_{nf}=T_s=T_{w1}, \quad q_1''=-k_{enf}\left.\frac{\partial T_{nf}}{\partial y}\right|_{y=-h_1}-k_{es}\left.\frac{\partial T_s}{\partial y}\right|_{y=-h_1} \tag{4d}$$

$$y=-h_2: \quad k_1\left.\frac{\partial T_1}{\partial y}\right|_{y=-h_2}=-q_1'' \tag{4e}$$

To obtain meaningful results, a reference concentration value at a specific point should be defined. Since the reference for the temperature field was defined at the inlet on the lower wall, the reference concentration at this point is set to C_0 and the following concentration boundary conditions are written.

$$y=-h_1 \quad C=C_0, \tag{5a}$$

$$y=0 \quad D\frac{\partial C}{\partial y}=D_T\frac{\partial T_{nf}}{\partial y}. \tag{5b}$$

Next, the following dimensionless parameters are introduced to enable further physical analysis.

$$\theta_i=\frac{2(T_i-T_{w,in})k_{es}}{(q_1''+q_2'')h_2}, \quad u_r=-\frac{h_2^2}{\mu_f}\frac{\partial p_{nf}}{\partial x}, \quad Bi=\frac{h_{sf}a_{sf}h_2^2}{k_{es}}, \quad \gamma=\frac{k_R h_1}{D},$$
$$Y=\frac{y}{h_2}, \quad Da=\frac{\kappa}{h_2^2}, \quad Br'=\frac{2\mu_{eff}\bar{u}^2}{(q_1''+q_2'')h_2}, \quad Sr=\frac{(q_1''+q_2'')h_1D_T}{2C_0k_{nf}D},$$
$$Y_1=\frac{h_1}{h_2}, \quad M=\frac{\mu_{eff}}{\mu_{nf}}, \quad k_{e1}=\frac{k_1}{k_{es}}, \quad Q=\frac{q_2''}{(q_1''+q_2'')},$$
$$X=\frac{x}{L}, \quad S=\frac{1}{\sqrt{MDa}}, \quad k_{e2}=\frac{k_2}{k_{es}}, \quad k=\frac{k_{enf}}{k_{es}}=\frac{\varepsilon k_{nf}}{(1-\varepsilon)k_s},$$
$$\xi=\frac{h_2}{L}, \quad Pr=\frac{C_{p,nf}\mu_{eff}}{k_{enf}}, \quad \Phi=\frac{C}{C_0}, \quad Re=\frac{2h_2\rho_{nf}\bar{u}}{\mu_{eff}},$$
$$U=\frac{u}{u_r}, \quad Pe=\frac{\bar{u}h_1}{D}, \tag{6}$$

where the dimensionless temperature follows the labelling convention; i = 1, 2,s, n_f.

2.3. Non-dimensionalisation and analytical solution

Eq. (1) can be non-dimensionalised using the parameters defined in Eqs. (6), resulting in

$$M\frac{d^2U}{dY^2}-\frac{U}{Da}+1=0 \quad -Y_1\leqslant Y<Y_1 \tag{7}$$

Similarly, the no slip boundary condition and the condition due to the axial symmetry at $Y=0$, can also be expressed in non-dimensional form as

$$U(\pm Y_1)=0, \tag{8a}$$

$$U'(0)=0. \tag{8b}$$

The solution of Eq. (7) then may be expressed by

$$U=Da\left(1-\frac{\cosh(SY)}{\cosh(SY_1)}\right). \quad -Y_1\leqslant Y<Y_1 \tag{9}$$

Using Eq. (8), the dimensionless average velocity across the channel can be calculated as

$$\bar{U}=Da\left(1-\frac{\tanh(SY_1)}{SY_1}\right). \tag{10}$$

By combining Eqs. (9) and (10) the following ratios are defined

$$u/\bar{u}=U/\bar{U}=\frac{SY_1(\cosh(SY_1)-\cosh(SY))}{SY_1\cosh(SY_1)-\sinh(SY_1)}. \tag{11}$$

Due to the assumption of fully developed flow and by incorporating the assumptions summarised in Section 2.1, the following conditions hold [32],

$$\frac{\partial T_{nf}}{\partial x}=\frac{d\bar{T}_{nf}}{dx}=\frac{\partial T_s}{\partial x}=\frac{d\bar{T}_s}{dx}=\frac{dT_{w1}}{dx}=\frac{dT_{w2}}{dx}=\Omega=\text{constant}. \tag{12}$$

Thus, the following form of solution is sought for the temperature equations:

$$T_i(x,y)=f_i(y)+\Omega x \quad i=1,2,s,nf, \tag{13}$$

where $f_i(y)$ is a function to be determined by solving Eqs. (2a)–(2d) in association with the given boundary conditions. In order to solve the transport of thermal energy in the porous medium, first it is necessary to add Eqs. (2b) and (2c) and then integrate the resultant equation over the cross-section of the channel. Substituting in the heat flux boundary conditions from Eqs. (4b) and (4d) yields

$$q_1''+q_2''+\frac{\mu_{nf}}{\kappa}\int_{-h_1}^{h_1}u^2dy+\mu_{eff}\int_{-h_1}^{h_1}\left(\frac{\partial u}{\partial y}\right)^2dy=\rho_{nf}C_{p,nf}\int_{-h_1}^{h_1}u\frac{\partial T_{nf}}{\partial x}dy. \tag{14}$$

Rearranging Eq. (11) allows substitution for u in Eq. (14). Applying the non-dimensional parameters, defined in Eqs. (6), facilitates the integration process to obtain

$$\frac{d\bar{T}_{nf}}{dx}=\frac{1}{2\rho_{nf}C_{p,nf}\bar{u}h_1h_2}\left[h_2q_1''+h_2q_2''+\frac{2\mu_{eff}S^3\bar{u}^2Y_1^2\cosh(SY_1)}{SY_1\cosh(SY_1)-\sinh(SY_1)}\right]=\Omega, \tag{15}$$

where the bulk mean temperature of the nanofluid is given by

$$\bar{T}_{nf}=\frac{1}{2\bar{u}h_1}\int_{-h_1}^{h_1}uT_{nf}dy. \tag{16}$$

Utilising the non-dimensional parameters of Eqs. (6) and the rearranged form of Eq. (11) together with Eq. (15) lead to the non-dimensional forms of Eqs. (2a-d). The constant coefficients are defined explicitly in Appendix B.

$$k_{e2}\theta_2''=0 \quad Y_1<Y\leqslant 1 \tag{17a}$$

$$k\theta_{nf}''+Bi(\theta_s-\theta_{nf})+D_2\cosh(2SY)+D_3\cosh(SY)+D_4=0 \quad -Y_1\leqslant Y<Y_1 \tag{17b}$$

$$\theta_s''-Bi(\theta_s-\theta_{nf})=0 \quad -Y_1\leqslant Y<Y_1 \tag{17c}$$

$$k_{e1}\theta_1''=0 \quad -1\leqslant Y<-Y_1 \tag{17d}$$

Algebraic manipulation of Eqs. (17b) and (17c), yields

$$k\theta_{nf}''''-Bi(1+k)\theta_{nf}''+(4S^2-Bi)D_2\cosh(2SY)+(S^2-Bi)D_3\cosh(SY)-BiD_4=0 \tag{18a}$$

$$k\theta_s''''-Bi(1+k)\theta_s''-Bi(D_2\cosh(2SY)+D_3\cosh(SY)+D_4)=0 \tag{18b}$$

Eqs. (4b) and (4d) along with Eqs. (17b) and (17c) allow for the calculation of the 8 boundary conditions of the two fourth order differential Eqs. (18a) and (18b). These equations are, however, linked to Eqs. (17a) and (17d), which then require further four boundary conditions in order for a solution to be obtained. Eqs. (4a, b, d, and e) provide the necessary extra boundary conditions. These give the following 12 boundary conditions required for the closure of the system:

$$\theta_{nf}(-Y_1)=\theta_s(-Y_1)=0, \quad \theta_{nf}(-Y_1)=\theta_s(-Y_1)=\theta_{w2}, \tag{19a, b}$$

$$\theta_s''(-Y_1)=\theta_s''(Y_1)=0,$$

$$\theta_{nf}''(-Y_1)=\theta_{nf}''(Y_1)=-\frac{1}{k}(D_2\cosh(2SY)+D_3\cosh(SY)+D_4), \tag{19c, d}$$

$$\theta_1(-Y_1)=0, \quad k_{e1}\theta_1'(1)=2(1-Q), \tag{19e, f}$$

$$\theta_2(Y_1)=\theta_{w2}, \quad k_{e2}\theta_2'(1)=2Q. \tag{19g, h}$$

Applying the boundary conditions given by Eqs. (19a-h) allows the analytical solutions of the system of Eqs. (17a), (17d), (18a), and (18b) to be found. The resultant closed-form dimensionless temperature profiles in the transversal direction are:

$$\theta_2(Y)=E_1+E_2Y \quad Y_1<Y\leqslant 1 \tag{20a}$$

$$\theta_{nf}(Y)=E_3\cosh(2SY)+E_4\cosh(SY)+E_5\cosh(\alpha Y)+E_6Y^2+E_7Y+E_8 \quad -Y_1\leqslant Y<Y_1 \tag{20b}$$

$$\theta_s(Y)=E_9\cosh(2SY)+E_{10}\cosh(SY)+E_{11}\cosh(\alpha Y)+E_6Y^2+E_7Y+E_{12} \quad -Y_1\leqslant Y<Y_1 \tag{20c}$$

$$\theta_1(Y)=E_{13}+E_{14}Y \quad -1\leqslant Y<-Y_1 \tag{20d}$$

in which

$$\alpha=\sqrt{Bi(1+k^{-1})}. \tag{21}$$

Through substitution of the dimensionless axial and transverse temperature profiles into Eq. (13), the final two-dimensional temperature profiles become

$$\theta_2(X,Y)=\frac{2X[1+Br'D_1S^2Y_1\cosh(SY_1)]}{Re\Pr kY_1\xi}+E_1+E_2Y \quad Y_1<Y\leqslant 1 \tag{22a}$$

$$\theta_{nf}(X,Y)=\frac{2X[1+Br'D_1S^2Y_1\cosh(SY_1)]}{Re\Pr kY_1\xi}+E_3\cosh(2SY)+E_4\cosh(SY)+E_5\cosh(\alpha Y)+E_6Y^2+E_7Y+E_8 \quad -Y_1\leqslant Y<Y_1 \tag{22b}$$

$$\theta_s(X,Y) = \frac{2X[1 + Br'D_1S^2Y_1\cosh(SY_1)]}{RePrkY_1\xi} + E_9\cosh(2SY) + E_{10}\cosh(SY) + E_{11}\cosh(\alpha Y) + E_6Y^2 + E_7Y + E_{12} \quad -Y_1 \leqslant Y < Y_1 \tag{22c}$$

$$\theta_1(X,Y) = \frac{2X[1 + Br'D_1S^2Y_1\cosh(SY_1)]}{RePrkY_1\xi} + E_{13} + E_{14}Y \quad -1 \leqslant Y < Y_1 \tag{22d}$$

where the expressions for $E_1 - E_{14}$ are provided in Appendix B.

2.4. Nusselt number and mass transfer

The heat transfer coefficients at the bottom and top walls of the channel are defined as

$$H_{w1} = \frac{q_1''}{T_{w1} - \bar{T}_{nf}}, \tag{23a}$$

$$H_{w2} = \frac{q_2''}{T_{w2} - \bar{T}_{nf}}. \tag{23b}$$

Thus, Nusselt number on the basis of the channel height h_1 is expressed and converted to dimensionless terms as follows,

$$Nu_{w1} = \frac{2H_{w1}h_1}{k_{enf}} = \frac{4(Q-1)Y_1}{k\bar{\theta}_{nf}}, \tag{24a}$$

$$Nu_{w2} = \frac{2H_{w2}h_1}{k_{enf}} = \frac{4QY_1}{k(\theta_{w2} - \bar{\theta}_{nf})}. \tag{24b}$$

The dimensionless bulk mean temperature of the nanofluid, $\bar{\theta}_{nf}$ may be found by determining a dimensionless form of Eq. (16) and then integrating over the channel. This yields

$$\bar{\theta}_{nf} = \frac{D_1}{2Y_1}\int_{-Y_1}^{Y_1}\theta_{nf}[\cosh(SY_1) - \cosh(SY)]dY. \tag{25}$$

Seeking a solution to the governing equation of mass transfer of the form:

$$C(x,y) = g(y) + h(x). \tag{26}$$

A control volume over a section of the channel with the length dx is considered and the thickness in the z direction is chosen to be 1. Application of the Taylor series expansion on a species balance written for this control volume leads to the following equation,

$$\left[\int_0^{h_1} u.Cdy\right] + K_R dx - \left[\int_0^{h_1} u.Cdy + \frac{\partial}{\partial x}\left(\int_0^{h_1} u.Cdy\right)dx\right] = 0. \tag{27}$$

Gathering terms and applying Leibniz rule leads to:

$$\int_0^{h_1} u\frac{\partial C}{\partial x}dy = K_R. \tag{28}$$

The velocity profile is symmetric over the channel and so the half channel may be used, thus the mean velocity across the half channel is given by:

$$\bar{u} = \frac{1}{h_1}\int_0^{h_1} udy. \tag{29}$$

Noting that the desired form of the solution means that $\frac{\partial C}{\partial x}$ does not rely on y and utilising Eq. (29) results in:

$$\frac{\partial C}{\partial x} = \frac{K_R}{h_1\bar{u}}. \tag{30}$$

Assigning C_0 as the initial concentration, the solution of Eq. (30) takes the form of

$$C(x) = \frac{K_R x}{h_1\bar{u}}. \tag{31}$$

Using the dimensionless parameters defined in Eqs. (6) then Eqs. (31) can be non-dimensionalised in the following form,

$$\Phi(X) = \frac{\gamma X}{PeY_1\xi} \tag{32}$$

Substitution of Eq. (30) into Eq. (3) gives

$$\frac{uK_R}{h_1\bar{u}} = D\frac{\partial^2 C}{\partial y^2} - D_T\frac{\partial^2 T_{nf}}{\partial y^2} \tag{33}$$

By employing the dimensionless parameters of Eqs. (6), and the velocity ratio of Eq. (11) allows Eq. (33) to be non-dimensionalised and rearranged in the form of

$$\Phi''(Y) = \frac{Srk}{Y_1\varepsilon}\theta_{nf}''(Y) + \frac{\gamma D_1(\cosh(SY_1) - \cosh(SY))}{Y_1^2}. \tag{34}$$

Since $\theta_{nf}''(Y)$ may be determined from Eq. (20b) only the boundary conditions Eqs. (5a) and (5b) require to be non-dimensionalised. These are expressed by,

$$\Phi'(0) = \frac{Srk}{Y_1\varepsilon}\theta_{nf}'(0) \tag{35a}$$

$$\Phi(-Y_1) = 1. \tag{35b}$$

Through applying Eqs. (35a) and (35b), Eq. (34) can be solved analytically to obtain the dimensionless concentration profile in the transverse direction. This reads

$$\Phi(Y) = F_1 + F_2Y + F_3Y^2 + F_4\cosh(2SY) + F_5\cosh(SY) + F_6\cosh(\alpha Y). \tag{36}$$

Finally, substituting Eqs. (36) and (32) into Eq. (26) gives the dimensionless concentration profiles in the axial and transverse directions,

$$\Phi(X,Y) = e\frac{\gamma X}{PeY_1\xi} + F_1 + F_2Y + F_3Y^2 + F_4\cosh(2SY) + F_5\cosh(SY) + F_6\cosh(\alpha Y). \tag{37}$$

Analytical expressions for $F_1 - F_6$ are lengthy and rather cumbersome and thus are not provided explicitly.

2.5. Entropy generation

The volumetric entropy generation for the system are expressed by [12,14,32],

$$\dot{S}_{w1}''' = \frac{k_1}{T_1^2}\left[\left(\frac{\partial T_1}{\partial x}\right)^2 + \left(\frac{\partial T_1}{\partial y}\right)^2\right], \tag{38a}$$

$$\dot{S}_S''' = \frac{k_{es}}{T_s^2}\left[\left(\frac{\partial T_s}{\partial x}\right)^2 + \left(\frac{\partial T_s}{\partial y}\right)^2\right] - \frac{h_{sf}a_{sf}(T_s - T_{nf})}{T_s}, \tag{38b}$$

$$\dot{S}_{nf}''' = \frac{k_{enf}}{T_{nf}^2}\left[\left(\frac{\partial T_{nf}}{\partial x}\right)^2 + \left(\frac{\partial T_{nf}}{\partial y}\right)^2\right] + \frac{h_{sf}a_{sf}(T_s - T_{nf})}{T_{nf}}, \tag{38c}$$

$$\dot{S}_{FF}''' = \frac{\mu_{nf}}{\kappa T_{nf}}u^2 + \frac{\mu_{eff}}{T_{nf}}\left(\frac{\partial u}{\partial y}\right)^2, \tag{38d}$$

$$\dot{S}'''_{DI} = \frac{RD}{C}\left[\left(\frac{\partial C}{\partial x}\right)^2 + \left(\frac{\partial C}{\partial y}\right)^2\right] + \frac{RD}{T_{nf}}\left[\left(\frac{\partial C}{\partial x}\right)\left(\frac{\partial T_{nf}}{\partial x}\right) + \left(\frac{\partial C}{\partial y}\right)\left(\frac{\partial T_{nf}}{\partial y}\right)\right], \tag{38e}$$

$$\dot{S}'''_{w2} = \frac{k_2}{T_2^2}\left[\left(\frac{\partial T_2}{\partial x}\right)^2 + \left(\frac{\partial T_2}{\partial y}\right)^2\right]. \tag{38f}$$

In Eqs. (38) entropy generation terms have been split into contributions from different sources of irreversibility. The terms $\dot{S}'''_{w1}$ and $\dot{S}'''_{w2}$ account for the entropy generation in the lower and upper thick walls respectively. Entropy generation in the solid phase of the porous medium due to heat transfer is accounted by $\dot{S}'''_{s}$, similarly $\dot{S}'''_{nf}$ accounts for the entropy generation rate in the nanofluid phase. The contribution made by the irreversibility due to flow friction is calculated as $\dot{S}'''_{FF}$. The term $\dot{S}'''_{DI}$ is the entropy generation caused by the combination of concentration gradients and also that by mixed thermal and concentration gradients.

To non-dimensionalise Eqs. (38a-f) the following parameters are required. These are the dimensionless entropy generation, dimensionless heat flux and an irreversibility distribution ratio respectively.

$$N_i = \frac{\dot{S}'''_i h_2^2}{k_{es}}, \quad i = w1, s, nf, FF, DI, w2 \tag{39}$$

$$\omega = \frac{(q''_1 + q''_2)h_2}{2k_{es}T_{w,in}} \tag{40}$$

$$\varphi = \frac{RDC_0}{k_{es}} \tag{41}$$

The resultant non-dimensionalised version of Eqs. (38a-f) are:

$$N_{w1} = \frac{k_{e1}\omega^2}{(\omega\theta_1 + 1)^2}\left[\left(\frac{\partial\theta_1}{\partial X}\right)^2 + \left(\frac{\partial\theta_1}{\partial Y}\right)^2\right] \quad -1 \leqslant Y < -Y_1 \tag{42a}$$

$$N_s = \frac{\omega^2}{(\omega\theta_s + 1)^2}\left[\xi^2\left(\frac{\partial\theta_s}{\partial X}\right)^2 + \left(\frac{\partial\theta_s}{\partial Y}\right)^2\right] - \frac{Bi\omega(\theta_s - \theta_{nf})}{(\omega\theta_s + 1)} \quad -Y_1 \leqslant Y < Y_1 \tag{42b}$$

$$N_{nf} = \frac{k\omega^2}{(\omega\theta_{nf} + 1)^2}\left[\xi^2\left(\frac{\partial\theta_{nf}}{\partial X}\right)^2 + \left(\frac{\partial\theta_{nf}}{\partial Y}\right)^2\right] + \frac{Bi\omega(\theta_s - \theta_{nf})}{(\omega\theta_{nf} + 1)} \quad -Y_1 \leqslant Y < Y_1 \tag{42c}$$

$$N_{FF} = \frac{D_2\omega}{(\omega\theta_{nf} + 1)}[\cosh^2(SY_1) - 2\cosh(SY)\cosh(SY_1) + \cosh(2SY)] \quad -Y_1 \leqslant Y < Y_1 \tag{42d}$$

$$N_{DI} = \frac{\varphi}{\Phi}\left[\xi^2\left(\frac{\partial\Phi}{\partial X}\right)^2 + \left(\frac{\partial\Phi}{\partial Y}\right)^2\right] + \frac{\varphi\omega}{(\omega\theta_{nf} + 1)}\left[\xi^2\left(\frac{\partial\Phi}{\partial X}\right)\left(\frac{\partial\theta_{nf}}{\partial X}\right) + \left(\frac{\partial\Phi}{\partial Y}\right)\left(\frac{\partial\theta_{nf}}{\partial Y}\right)\right] \quad -Y_1 \leqslant Y < Y_1 \tag{42e}$$

$$N_{w2} = \frac{k_{e2}\omega^2}{(\omega\theta_2 + 1)^2}\left[\left(\frac{\partial\theta_2}{\partial X}\right)^2 + \left(\frac{\partial\theta_2}{\partial Y}\right)^2\right] \quad Y_1 \leqslant Y < 1 \tag{42f}$$

To facilitate the study of entropy generation and compare the contributions from different sources of irreversibility, the equations for the nanofluid and the solid phases of the porous medium are broken down. This provides the following equations for the irreversibility of heat transfer in the system.

$$N_{s,ht} = \frac{\omega^2}{(\omega\theta_s + 1)^2}\left[\xi^2\left(\frac{\partial\theta_s}{\partial X}\right)^2 + \left(\frac{\partial\theta_s}{\partial Y}\right)^2\right], \tag{43a}$$

$$N_{nf,ht} = \frac{k\omega^2}{(\omega\theta_{nf} + 1)^2}\left[\xi^2\left(\frac{\partial\theta_{nf}}{\partial X}\right)^2 + \left(\frac{\partial\theta_{nf}}{\partial Y}\right)^2\right]. \tag{43b}$$

By adding the components of Eqs. (42b) and (42c) the interstitial volumetric entropy generation term can be expressed by,

$$N_{int} = \frac{Bi\omega^2(\theta_{nf} - \theta_s)^2}{(\omega\theta_s + 1)(\omega\theta_{nf} + 1)}. \tag{44}$$

The volumetric entropy generations for the porous insert, N_{pm} is simply the sum of the equations that are applicable to the porous medium. This is a function defining the entropy generation for the combined processes of heat transfer, viscous dissipation, and concentration gradients for any given points (X, Y).

$$N_{pm} = N_{s,ht} + N_{nf,ht} + N_{int} + N_{FF} + N_{DI}. \tag{45}$$

For the total entropy generation in the microreactor, N_{Tot}, the sum of the parts of volumetric entropy generation in the ranges in which they are valid is integrated over the volume of the channel. The contributions from the walls are then added. This gives a numerical value for the total entropy for any given configuration, and is obtained using the following equation

$$N_{Tot} = \int_{-1}^{1}\int_{0}^{1}\sum N_i dX dY, \quad i = w1, s, nf, FF, DI, w2. \tag{46}$$

2.6. Validation

Appendix C shows that the analytical solution of the temperature fields developed in Section 2.3 can be rigorously reduced to those of Ting et al. [32] for a two-dimensional porous channel. This is achieved by ignoring the catalytic surfaces and approaching the wall thicknesses to zero such that the configuration shown in Fig. 1 is converted to that in Ref. [32] in the absence of internal heat generation.

3. Results and discussions

The problem solved in Section 2 features a large number of dimensionless parameters. To conduct quantitative analyses default values are assigned to them in Table 1.

3.1. Temperature fields

Figs. 2–5 show contours of the dimensionless temperatures plotted for the entire duct. The non-dimensional temperature fields of the nanofluid and porous solid phases are shown and the figures do not include the temperature distributions inside the solid walls. It should be noted that the dimensionless temperature defined in Eqs. (6) is on the basis of the wall temperature at the inlet of the duct. Hence, both negative and positive dimensionless temperatures may exist throughout the duct. Fig. 2 depicts the variation of the solid and nanofluid temperature fields for different values of thermal conductivity of the lower wall. Other parameters have been given in Table 1. The asymmetric behaviour of the dimensionless temperature fields is evident in this figure. This is primarily due to the imbalance in the thermal loads applied to the top and bottom external surfaces of the system. It is also due to the variations in the thermal conductivity of the lower wall, which changes the thermal resistance of this wall and hence can contribute with the asymmetry of the temperature profiles. Fig. 2a and b show that there exists a considerable temperature

Table 1
Default values of the dimensionless parameters used in the figures.

Dimensionless parameter	Default value	Dimensionless parameter	Default value
ϕ	2%	k	0.05
Bi	1	k_{e1}	0.5
Br'	0.01 0.00001 (Entropy analysis)	k_{e2}	0.5
γ	1	Q	0.75
Da	0.1	ω	0.001
Pe	10	φ	0.01
Pr	5	Y_1	0.8
Re	150	X_0	0.1
Sr	0.7	ξ	0.05
ε	0.95		

difference between the wall and the nanofluid at the inlet of the duct. This is depicted by a relatively large negative dimensionless temperature at the entrance of the microchannel. Continuous heating results in increase of the solid and nanofluid temperatures, which in turn pushes the dimensionless temperatures towards zero and positive values. When the values of thermal conductivity of the lower wall increase, the sign change in the dimensionless temperatures occurs earlier along the duct. Fig. 2c and d show that as the thermal conductivities of the wall increases a larger fraction of the duct volume features small values of dimensionless temperatures. This behaviour implies that the temperature differences between the solid and fluid phases at the inlet of the duct are lower at higher thermal conductivities of the wall. This is to be expected, as enhancing the thermal conductivity of the wall reduces its thermal resistance and results in lowering the required temperature differences for the transfer of the imposed thermal load to the nanofluid. Fig. 2 also reflects the significant difference between the temperature fields in the nanofluid and porous solid phase. Such difference highlights the importance of the undertaken LTNE approach.

Fig. 3 shows the contours of the dimensionless temperatures for different values of the porous solid conductivity. It is clear in this figure that for low conductivity values of the porous solid (Fig. 3a and b) the change of dimensionless temperature through the pipe is minimal. By increasing the thermal conductivity of the porous solid, the nanofluid and solid phases both experience more extensive variations in their non-dimensional temperatures. Fig. 4 illustrates the influences of the wall thickness upon the dimensionless temperature fields. It is evident from this figure that by thickening the wall (decreasing the value of Y_1) the variations in the dimensionless temperatures are intensified. This could be readily verified by comparing Fig. 4a and c or b and d. In particular, for the thicker walls the solid and nanofluid phases experience greater temperature differences. This result is consistent with the physical intuition, which requires larger temperature differences for thicker and more resistive walls. It is also in keeping with the recent results in Refs. [12–14], which reported one-dimensional analyses of heat transfer in microreactors. Most importantly, the behaviour

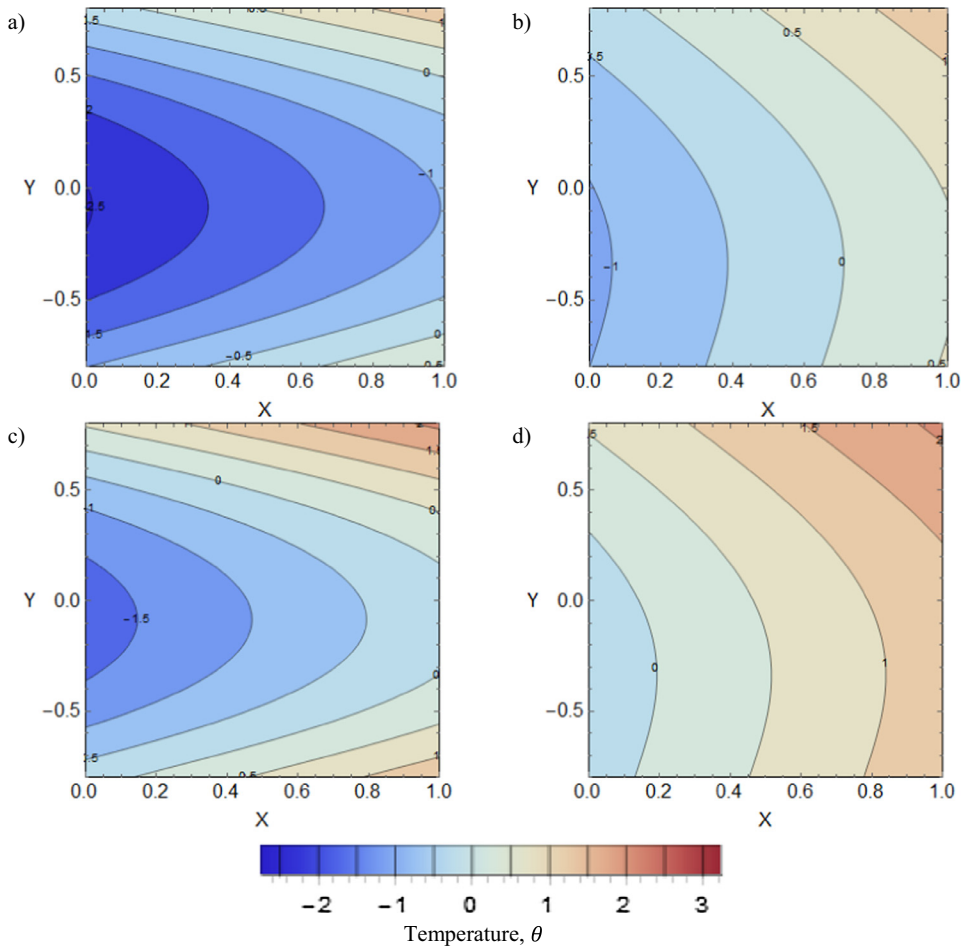

Fig. 2. Temperature contours for varying lower wall thermal conductivity, k_{e1}, (a, and c) nanofluid phase with k_{e1} values of 0.1, and 0.5, respectively. (b and d) solid phase with k_{e1} values of 0.1, and 0.5, respectively.

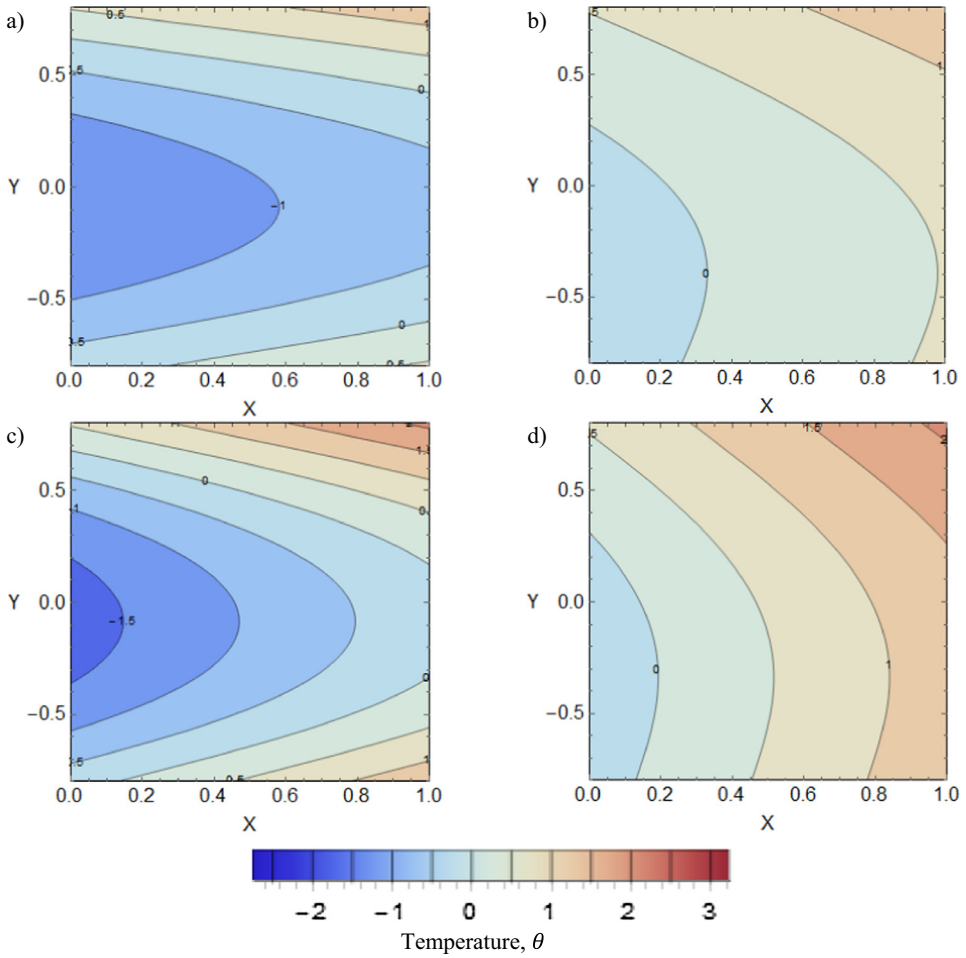

Fig. 3. Temperature contours for varying thermal conductivity of the porous solid, k_s (a), and (c) nanofluid phase with k_s values of 100, and 200 W/m K, respectively. (b), and (d) porous solid phase with k_s values of 100, and 200 W/m K, respectively.

observed in Fig. 4 is of practical significance in the design of microreactors as it clearly shows the major effects of wall thicknesses on the temperature fields inside the reactor. Such effects are often negligible in macro-reactors. Nonetheless, the similarity of channel diameter and wall thickness in microsystems imparts a pronounced effect on the thermal behaviour of these systems. The effects of strengthening the imbalance in the exposed thermal fluxes are investigated in Fig. 5. This figure shows that, as expected, magnifying the heat flux (q_2'') on the upper wall increases the asymmetry of the temperature fields. It also shows that the temperature gradients near the upper wall have increased to enable transversal transfer of stronger heat loads to the nanofluid and solid phases.

It should be recalled that in practice, temperature is amongst the most essential characteristics of any chemical system. The results presented in this subsection showed that the configuration of the microstructure, as well as the thermophysical properties of the porous solid can majorly affect the thermal behaviour of the microreactor.

3.2. Nusselt number and concentration fields

Fig. 6 shows the variations of Nusselt number on the upper and lower internal walls of the channel against the changes in the lower wall thickness. As a general trend, this figure shows that the numerical value of Nusselt number increases significantly by reducing the thickness of the lower wall. This is a clear manifestation of the significant role of the microstructure in the thermal behaviour of microsystems and has been also emphasised in other recent studies [12]. Fig. 6a depicts the sensitivity of Nusselt number to the thermal conductivity of the porous solid. As expected, increases in the value of thermal conductivity of the solid phase of the porous medium results in enhancement of the Nusselt number. The effects of thermal load imbalance (Q defined in Eq. (6)) on the Nusselt number have been investigated in Fig. 6b. According to this figure as the value of Q approaches unity, the Nusselt number increases. The effects of permeability of the porous medium on the rate of heat transfer have been shown in Fig. 6c. In keeping with the findings of other investigations [24], this figure shows that the Nusselt number increases at lower values of Darcy number. Fig. 6d shows the response of Nusselt number to changes in the volumetric concentration of nanoparticles. A modest improvement is observed in Nusselt number by increases in the volumetric concentration of nanoparticles. This is in total agreements with the findings of the recent studies of forced convection of nanofluids in porous media [26,48].

Figs. 7 and 8 show the concentration contours throughout the entire channel (part a) and also for a selected segment (parts b, c and d). These figures clearly demonstrate the axial increase of the concentration due to catalytic activities and the subsequent advection of species by the flow. Fig. 7 illustrates the effects of increase in Damköhler number on the concentration field. Parts b, c and d of this figure indicate that the axial gradient of the concentration field is enhanced as the numerical value of Damköhler

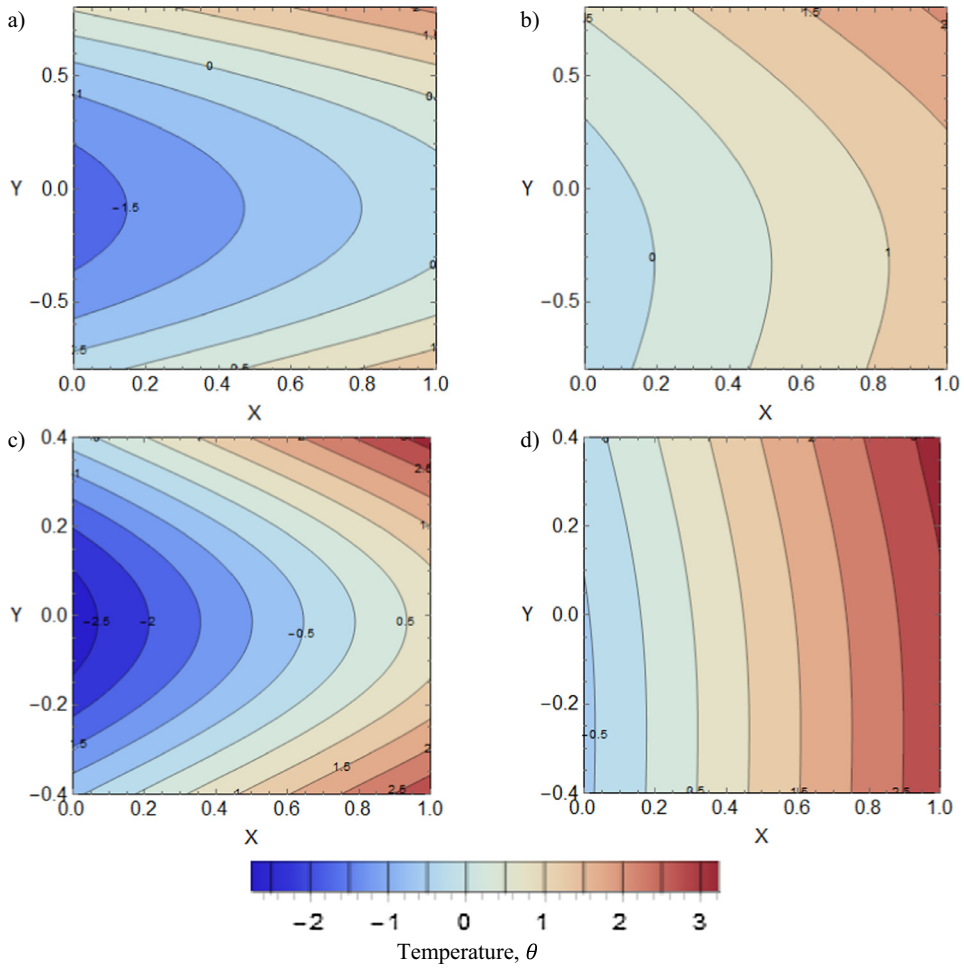

Fig. 4. Temperature contours for varying wall thickness, Y_1, (a), and (c) nanofluid phase with Y_1 values of 0.8, and 0.4, respectively. (b), and (d) porous solid phase with Y_1 values of 0.8, and 0.4, respectively.

number increases. This is to be expected, as Damköhler number correlates with the reaction rate on the surface of catalyst and hence it is a measure of chemical activity of the system. Fig. 7 also shows that by increasing Damköhler number the transversal gradient of concentration increases. This can be verified by comparing the variations of concentration from the lower or upper wall to the central axis of the channel in Fig. 7b, c and d. Similar behaviours are observed in Fig. 8, which depicts the response of the concentration field to the changes in Soret number. A notable feature of Figs. 7 and 8 is the symmetricity of the concentration contours. The transport of mass is coupled to that of heat through Soret effect (see Eq. (3)) and Figs. 2–5 showed the highly asymmetric character of the temperature contours. It may be, therefore, expected that the distribution of concentration contours should be also asymmetric. However, it is important to note that only the second derivative of temperature appears in Eq. (3). This tends to smear out the asymmetry of the temperature and results in mostly symmetric concentration contours shown in Figs. 7 and 8.

3.3. Local and total entropy generation

A detailed study of local entropy generation is presented in Figs. 9–12. Each figure includes 6 sub-figures demonstrating different terms in Eq. (45). This division is on the basis of the work of Ting et al. [32] and extends that to mass transferring flows by including N_{DI} term. It should be stated that in these figures, only the microchannel has been considered and the irreversibilities of the two solid walls have been excluded. Fig. 9 shows the contours of local entropy generation for the default conditions set in Table 1. In this figure, the asymmetric behaviour of entropy generation by intra-phase heat transfer in solid and nanofluid phase is in keeping with those observed in temperature contours presented in Figs. 2–5. Interestingly, however, the irreversibility associated with the interphase heat transfer between the porous solid and nanofluid is more symmetric, which indicates that the interphase heat transfer is largely unaffected by the asymmetry of the problem.

Fig. 9d shows the local entropy generation by the hydrodynamic irreversibilities. The highly irreversible regions in the vicinity of the walls and around the centreline of the channel are quite noticeable in this figure. The former is because of the enhanced viscous effects in the near wall region, while the latter is due to the higher velocity of the fluid around the centreline of the microchannel. It is noted that a very similar behaviour of hydrodynamic irreversibility was reported by Ting et al. [32] with the same order of magnitude as that shown in Fig. 9d. It should be emphasised here that the inclusion of viscous dissipation terms in heat transport equation has a major influence on the magnitude of this source of irreversibility. Exclusion of this effect often renders the entropy generation by fluid flow rather negligible in comparison with the irreversibility of heat transfer [49]. However, Fig. 9 shows that hydrodynamic and heat transfer irreversibilities in nanofluid phase are of the same order of magnitude and therefore of comparable

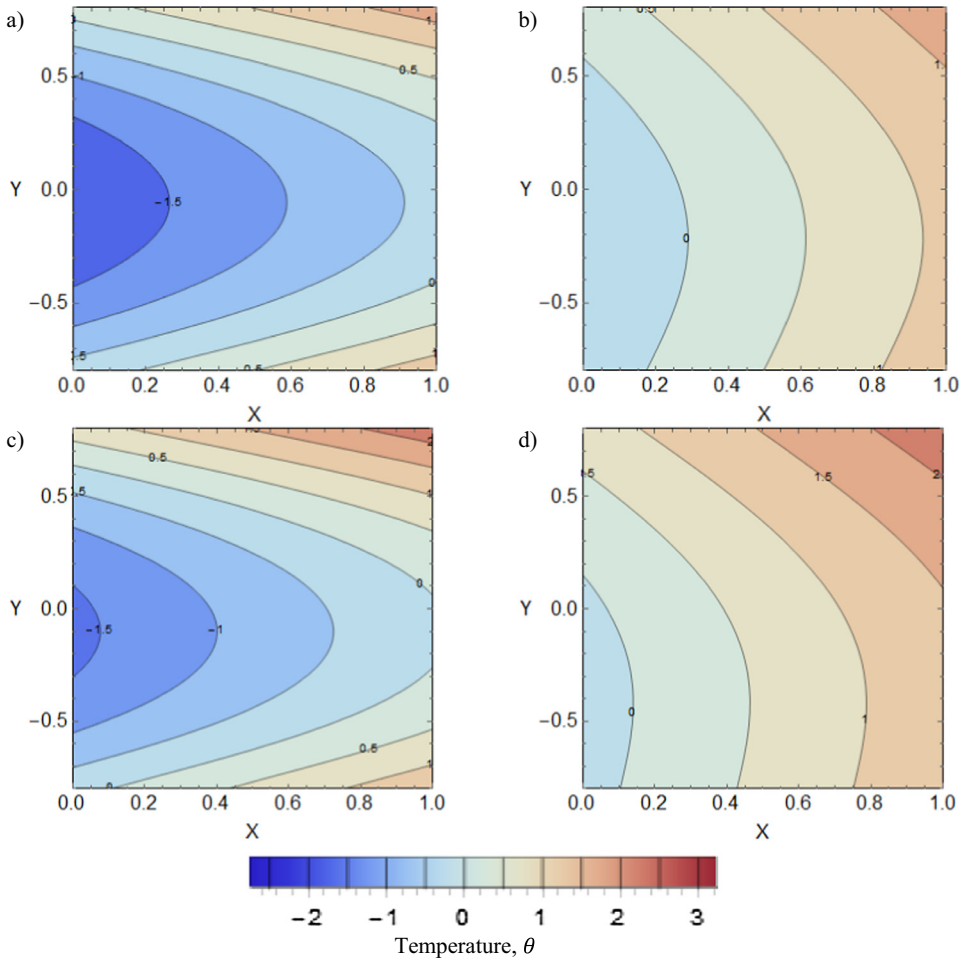

Fig. 5. Temperature contours for varying heat flux ratio, Q, (a), and (c) nanofluid phase with Q values 2/3, and 4/5, respectively. (b), and (d) porous solid phase with Q values 2/3, and 4/5, respectively.

significance. This conclusion was also made by Ting et al. [32]. Fig. 9e shows the contours of local entropy generation by mass transfer. There are two distinctive features in this figure. First, the general configurations of the contours are different to those of other sub-figures and are correlated with the diffusive-advected nature of mass transfer from the catalytic surfaces. Second, the magnitude of mass transfer irreversibility appears to be much larger than other sources of irreversibility. As a result, the overall local irreversibility is completely dominated by entropy generation through mass transfer.

Although not shown in here, an extensive parametric study revealed that the dominance of mass transfer irreversibility prevails for a large part of the parametric space. For this reason, Fig. 10 only includes the contours of local entropy generation by mass transfer. Fig. 10a depicts the effects of decreasing the permeability of the medium compared to the default value of Darcy number in Table 1. A comparison between this figure and Fig. 9e indicates that the resultant flow modification has affected the distribution of local entropy generation. This is to be anticipated as mass transfer is highly influenced by advection and therefore changes in the flow affect the irreversibility of mass transfer. The effect of increasing Damköhler number has been considered in Fig. 10b. In agreement with the arguments made about Figs. 7 and 8, magnifying Damköhler number intensifies the mass transfer rate and hence increases the associated irreversibility. Increasing the thermal conductivity ratio in Fig. 10c leads to an interesting effect. Here the transversal gradient of the local entropy generation has increased in comparison to that in Fig. 9e. However, the axial gradient of the local entropy generation shows a considerable decline with respect to the base case. This is particularly the case for areas between the walls and the centreline of the microchannel. An important behaviour is observed in Fig. 10d, wherein the thickness of the wall has been doubled in comparison with the default value in Table 1. It is noted that the local entropy generation in this sub-figure is one order of magnitude larger than any other sub-figure in Fig. 10. Once again, this reflects the significance of the wall thickness or microstructure configuration in the thermal and entropic responses of the microreactors. Fig. 10e and f show the influences of imbalance in the imposed heat flux (Q) and Soret number, respectively. It appears that Q has modest effects on the local entropy generation, while the influences of Soret number are more pronounced.

The preceding discussion may imply that in the current problem the mass transfer irreversibilities are always the most significant source of entropy generation. However, this will be an incorrect generalisation and there exist situations in which entropy generation by mass transfer is very much comparable with other sources of irreversibility. Figs. 11 and 12 illustrate two examples of such situations. In Fig. 11, the microchannel has been exposed to a high thermal load represented by a significant increase in ω compared to the default values. This has led to a major boost in the heat transfer irreversibility, shown in Fig. 11a–c, which has subsequently intensified the entropy generation by fluid flow,

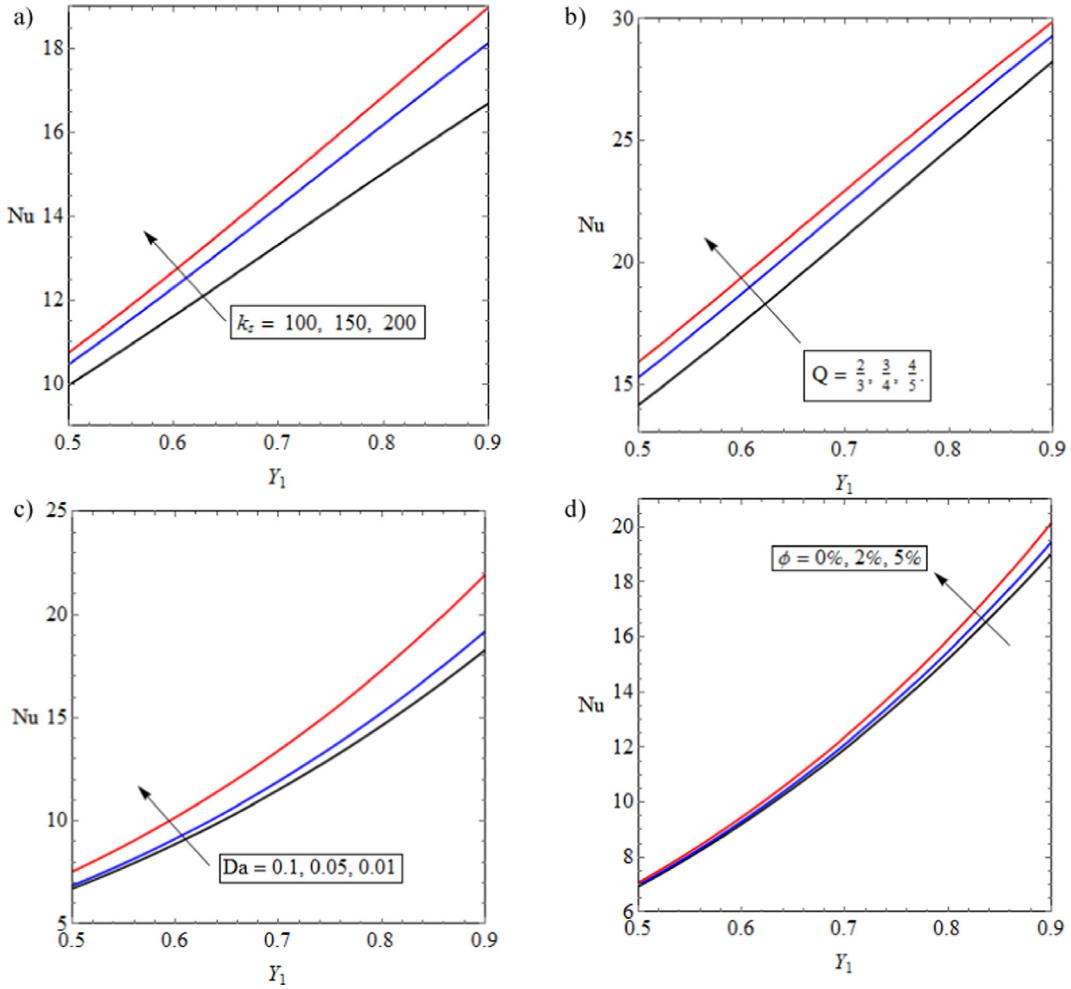

Fig. 6. Nusselt number versus the lower wall thickness, Y_1 (a) on the upper wall and for different values of thermal conductivity of the porous medium, k_s (W/m K) (b) on the upper wall and different values of Q, (c) on the lower wall and different values of Darcy number, (d) on the lower wall and different volumetric concentration of nanoparticles.

shown in Fig. 11d. Yet, entropy generation by mass transfer remains within the same order of magnitude as the default case (Fig. 9). Consequently, the overall local entropy generation, shown in Fig. 11f, is no longer dominated by the irreversibility of mass transfer. In fact, in this case the additive effect of entropy generations by heat transfer is the most significant source of entropy generation. Fig. 12 illustrate a particular case with zero Soret number. Part e of this figure shows that by excluding the thermal diffusion of mass the numerical value of entropy generation by mass transfer declines by about three orders of magnitude. As a result, in Fig. 12 entropy generation by heat and mass transfer are of the same order of magnitude. This clearly shows the essential role of coupled heat and mass transfer in entropy generation and identifies the Soret effect as a major contributor to the total irreversibility encountered in the microreactor.

The total entropy generation within the system is the sum of the five different sources of irreversibility within the microchannel plus entropy generation in the solid walls, see Eq. (46). The total entropy generation is a measure of irreversibility of the whole system and is therefore of obvious practical significance. Figs. 13 and 14 depict the variations of the total entropy generation within the system against a number of parameters. Fig. 13 illustrates the effects of Soret number on the total generation of entropy. In Fig. 13a, the total entropy generation has been plotted against the dimensionless heat flux and for different values of Soret number. This figure shows a positive correlation between the total entropy generation and the non-dimensional heat flux. It also indicates that for all values of non-dimensional heat flux, magnification of Soret number intensifies the total generation of entropy. A similar trend is observed in Fig. 13b in which total entropy increases with increasing the thermal conductivity ratio and Soret number.

Fig. 13c reveals the interactions between the irreversibilities of the two mechanisms of mass transfer. This figure shows the total entropy generation in a range of Damköhler number and for a few discrete values of Soret number. For Soret number of zero, and thus no thermal diffusion of mass, the total entropy generation increases monotonically with Damköhler number. Introducing a finite Soret number results in increasing the total generation of entropy. Nonetheless, the monotonic trend in increasing the total entropy through increasing Damköhler number remain unchanged. Fig. 13d indicates that the total entropy generation within the system is significantly affected by the variations in the thickness of the microchannel walls. It should be clarified here that based upon the definitions provided in Eq. (6), increasing Y_1 implies a decrease in the thickness of the microchannel. Thus, Fig. 13d indicates that through increasing the thickness of the wall the total irreversibility of the system is intensified quite significantly. Once again, Soret number acts in favour of magnifying the total entropy generation.

Fig. 14 shows the variations of total entropy generation with non-dimensional heat flux groups of ω and *Re*. Fig. 14a

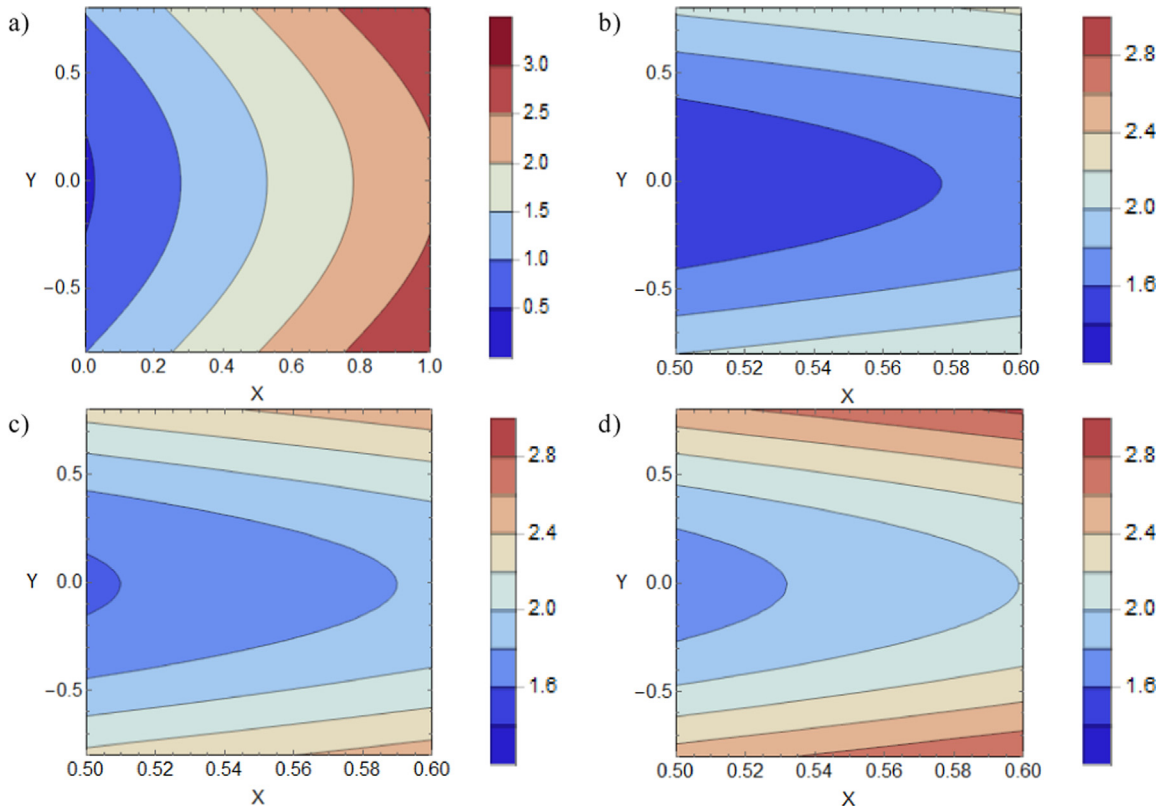

Fig. 7. Concentration contours for varying Damköhler number, γ, (a) the full channel for $\gamma = 0.8$, (b) mid-section of the channel, for $\gamma = 0.8$, (c) mid-section for $\gamma = 1.0$, and (d) mid-section for $\gamma = 1.2$.

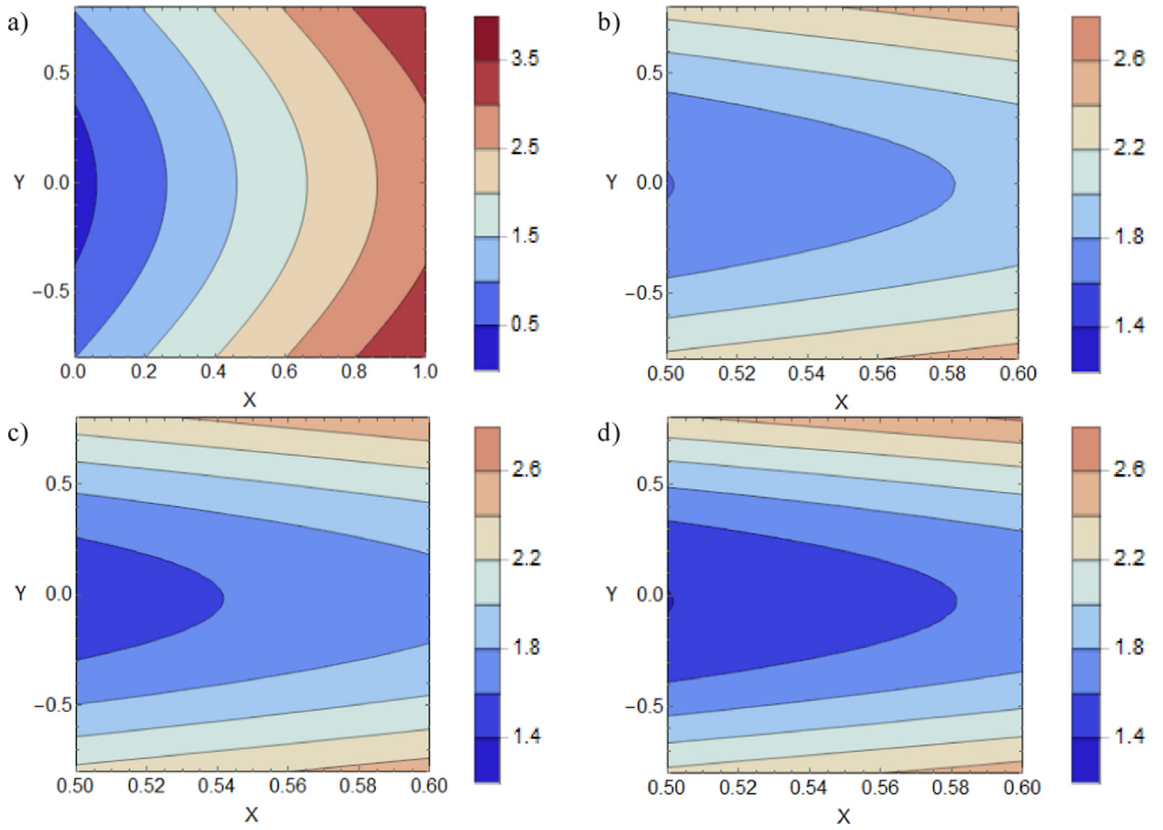

Fig. 8. Concentration contours for varying Soret number, *Sr*, (a) the full channel for $Sr = 0.5$, (b) mid-section of channel, for $Sr = 0.5$, (c) mid-section for $Sr = 0.7$, and (d) mid-section for $Sr = 0.9$.

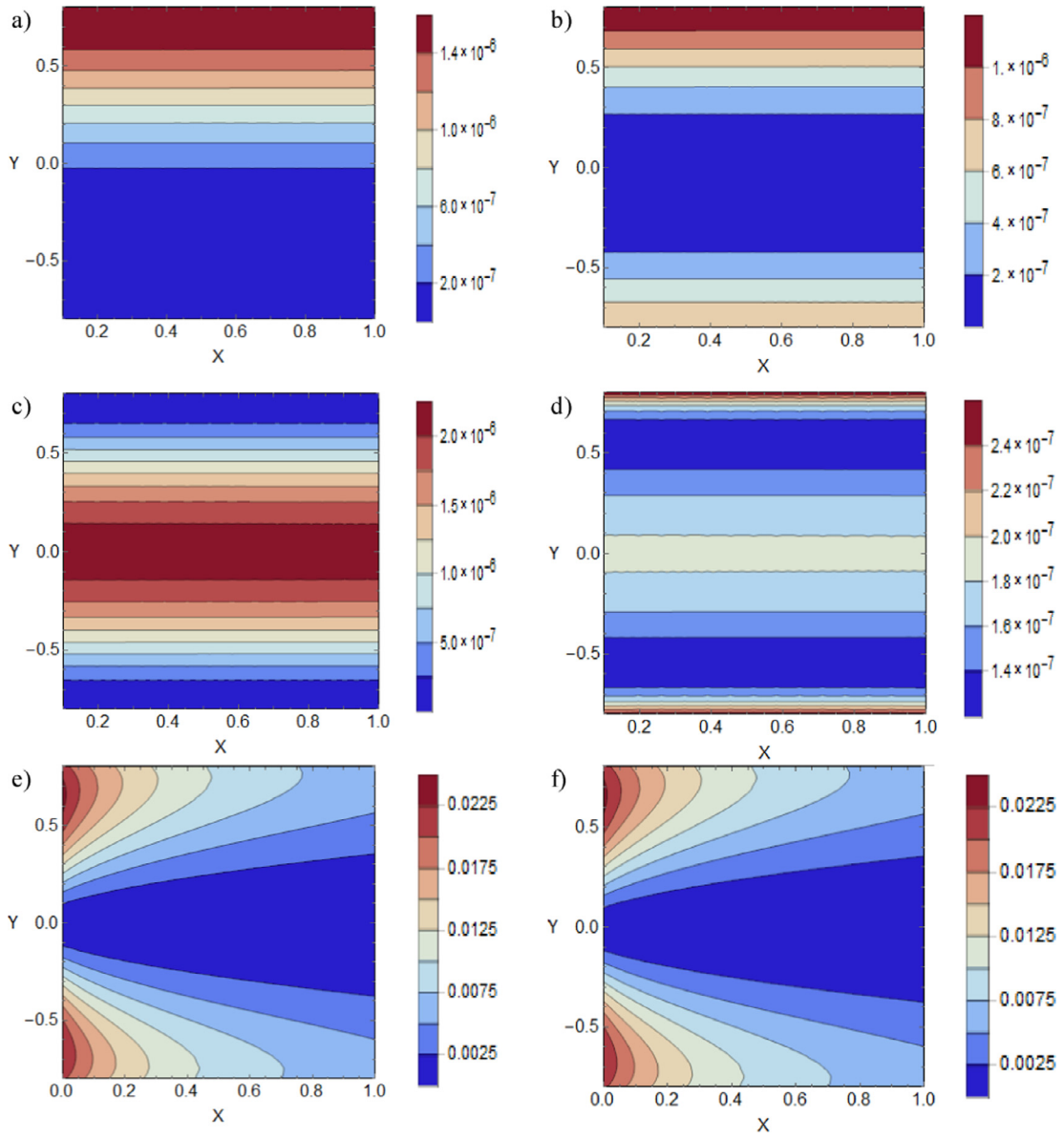

Fig. 9. Entropy contours for the base configuration (Table 1) (a) $N_{s,ht}$, (b) $N_{nf,ht}$, (c) N_{int}, (d)N_{FF}, (e) N_{DI} and (f) N_{pm}.

demonstrates the strong correlation between the total entropy generation and the dimensionless heat flux. This figure also indicates that for any fixed value of ω, the total entropy increases significantly by magnifying the value of Damköhler number. Fig. 14b shows that the changes of total entropy generation with the Reynolds number (defined in Eq. (6)) can include an extremum point. This figure clearly shows the dual effects of Reynolds number upon the total irreversibility of the system. For very small values of Reynolds number, the entropy generation is large. This is because of the fact that under small flow rates the forced convection mechanism is highly suppressed and therefore the system in Fig. 1 builds up in temperature and becomes highly irreversible. Increasing Reynolds number brings down the total irreversibility sharply and leads to the formation of a local minimum point. Any increase of Reynolds number beyond this point slightly increases the total irreversibility as the hydrodynamic irreversibilities start to become noticeable.

4. Conclusions

A two-dimensional analytical model of transport of heat and mass and also generation of entropy was developed for a microreactor featuring catalytic surfaces and exposed to uneven thermal fluxes. The microreactor was filled by a porous material and the solid thick walls were taken into account to represent the microstructure of the reactor. The analysis let the porous medium be under LTNE and also considered the thermal diffusion of mass and viscous dissipation of momentum. The results were presented in the form of contour plots of temperature, concentration and local entropy generation fields. These visualised the transversal diffusion of heat and mass and the simultaneous advection of them in the investigated asymmetric microsystem. Further, the Nusselt number on the internal surfaces of the microchannel and the total entropy generation within the entire system were calculated. The key findings of this work can be summarised as follows.

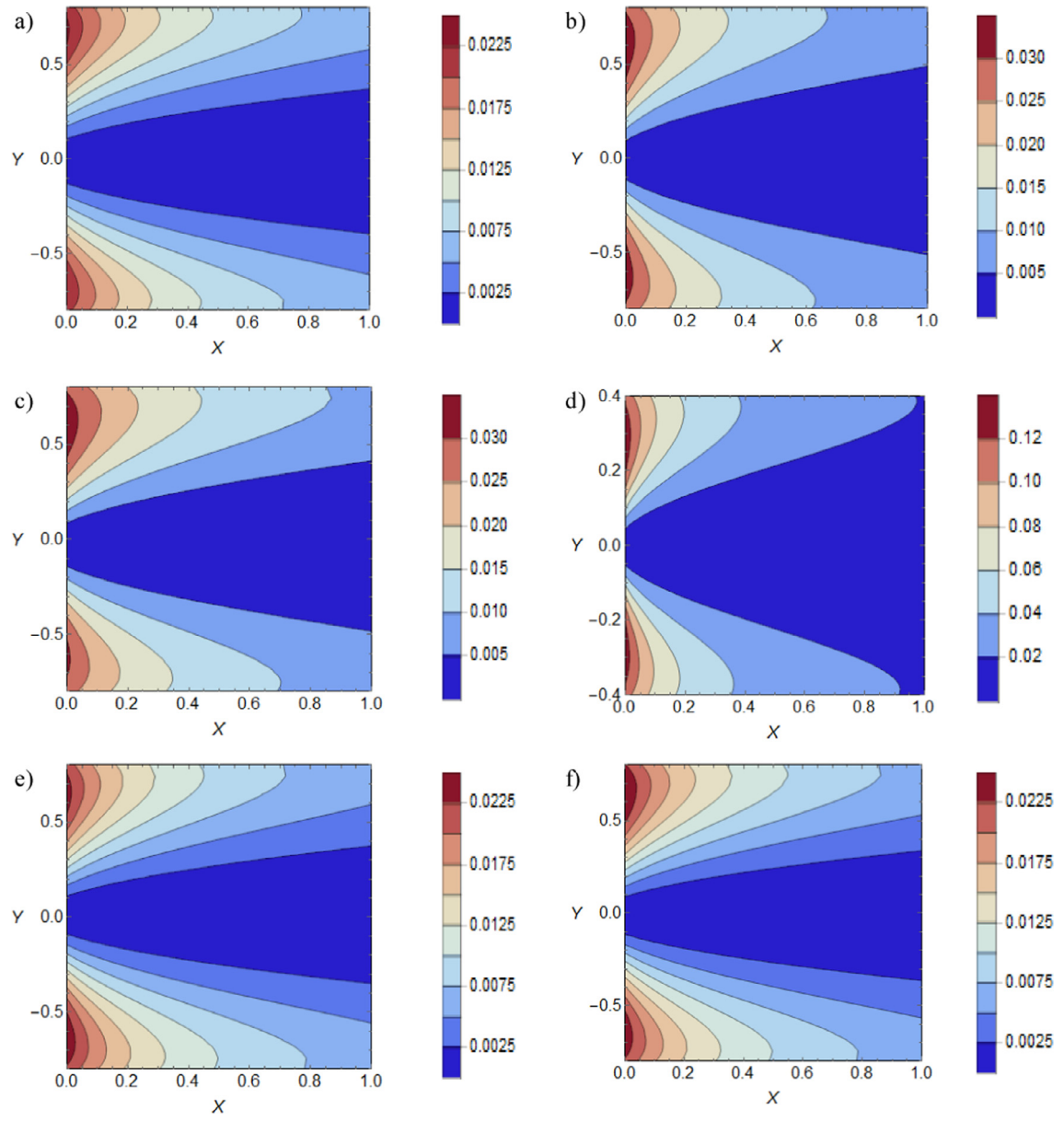

Fig. 10. Contours of local entropy generation by mass transfer, N_{DI}, (a) $Da = 0.05$, (b) $\gamma = 1.2$, (c) $k = 0.2$, (d) $Y_1 = 0.4$, (e) $Q = 0.2$, (f) $Sr = 0.9$.

- The developed mathematical model provides a two-dimensional, analytical solution of the temperature and concentration fields in the microreactor. These are of high significance in the reactor design and, process control and optimisation.
- While there is a long list of parameters that can affect the temperature fields, the wall thicknesses of the microstructure were found most influential in altering the temperatures of the nanofluid and porous solid phases.
- The Nusselt number on the upper and lower internal walls were shown to be strongly dependent upon the thickness of the walls. In general, increasing the wall thickness results in significant reduction of Nusselt number.
- For most combination of parameters, the irreversibility of mass transfer and in particular that of Soret effect is the dominant sources of entropy generation within the microreactor. Nonetheless, this is not the case for elevated values of imposed heat flux, which result in magnification of thermal irreversibility.
- The total entropy generation within the system was found to be monotonically increasing with the thermal conductivity ratio and the wall thickness. Similarly, Soret and Damköhler numbers were shown to be very influential in increasing the total entropy generation inside the microreactor. Minimisation of the total entropy generation may be sought by varying the value of Reynolds number.

These points are of clear relevance to the design of more efficient microreactors. Further, the analytical models presented in this work can be used for validation of the future numerical simulations of microreactors.

Conflict of interest

The authors declare no conflicts of interest.

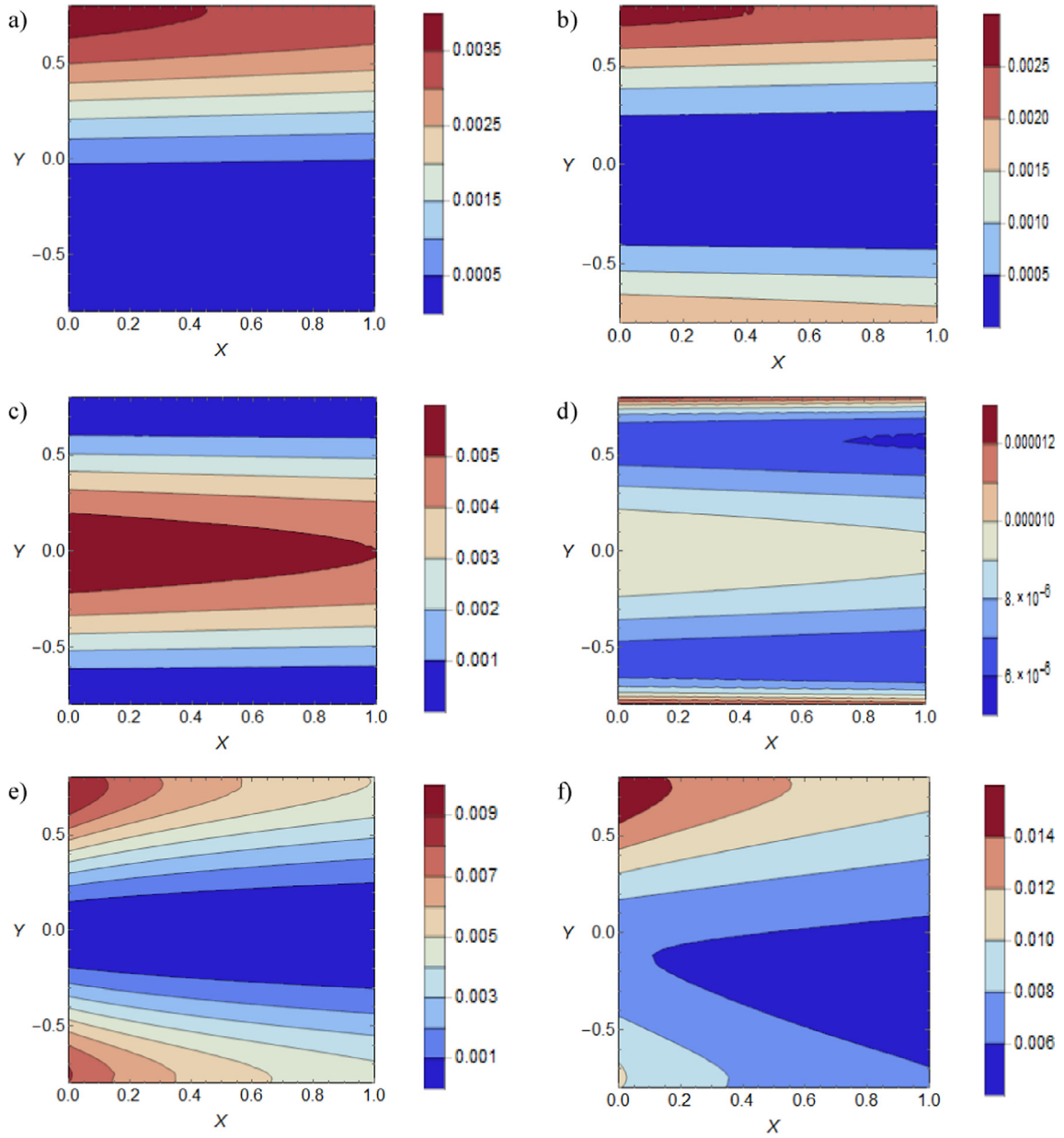

Fig. 11. Entropy contours for heat flux, $\omega = 0.05$, (a) $N_{s,ht}$, (b) $N_{nf,ht}$, (c) N_{int}, (d) N_{FF}, (e) N_{DI} and (f) N_{pm}.

Acknowledgment

G. Hunt gratefully acknowledges the financial support of the University of Glasgow through EPSRC DTA (G. Hunt) funding award number EP/M506539/1.

Appendix A. Thermophysical properties of the nanofluid

The effective viscosity for a nanofluid is modelled as a dilute suspension of small rigid spheres in a base fluid is defined by Brinkman [52] as:

$$\mu_{nf} = \frac{\mu_f}{(1-\phi)^{2.5}}, \tag{A1}$$

where ϕ is the volume fraction of the nanoparticles. The ratio of the effective thermal conductivity of the nanofluid to the thermal conductivity of the base fluid allows the former to be approximated using the Maxwell-Garnetts model [53]. That is

$$\frac{k_{nf}}{k_f} = \frac{k_p + 2k_f - 2\phi(k_f - k_p)}{k_p + 2k_f + \phi(k_f - k_p)} \tag{A2}$$

while the effective density and specific heat are defined as follows [53]:

$$\rho_{nf} = \rho_f(1-\phi) + \rho_p, \tag{A3a}$$

$$(\rho C_p)_{nf} = (\rho C_p)_f(1-\phi) + (\rho C_p)_p\phi. \tag{A3b}$$

Appendix B. Closed form constants

Provided here is a list of the closed form constants $D_1 - D_4$ and $E_1 - E_{14}$ pertinent to Eqs. (17) and (22).

$$D_1 = \frac{SY_1}{SY_1\cosh(SY_1) - \sinh(SY_1)} \tag{B1a}$$

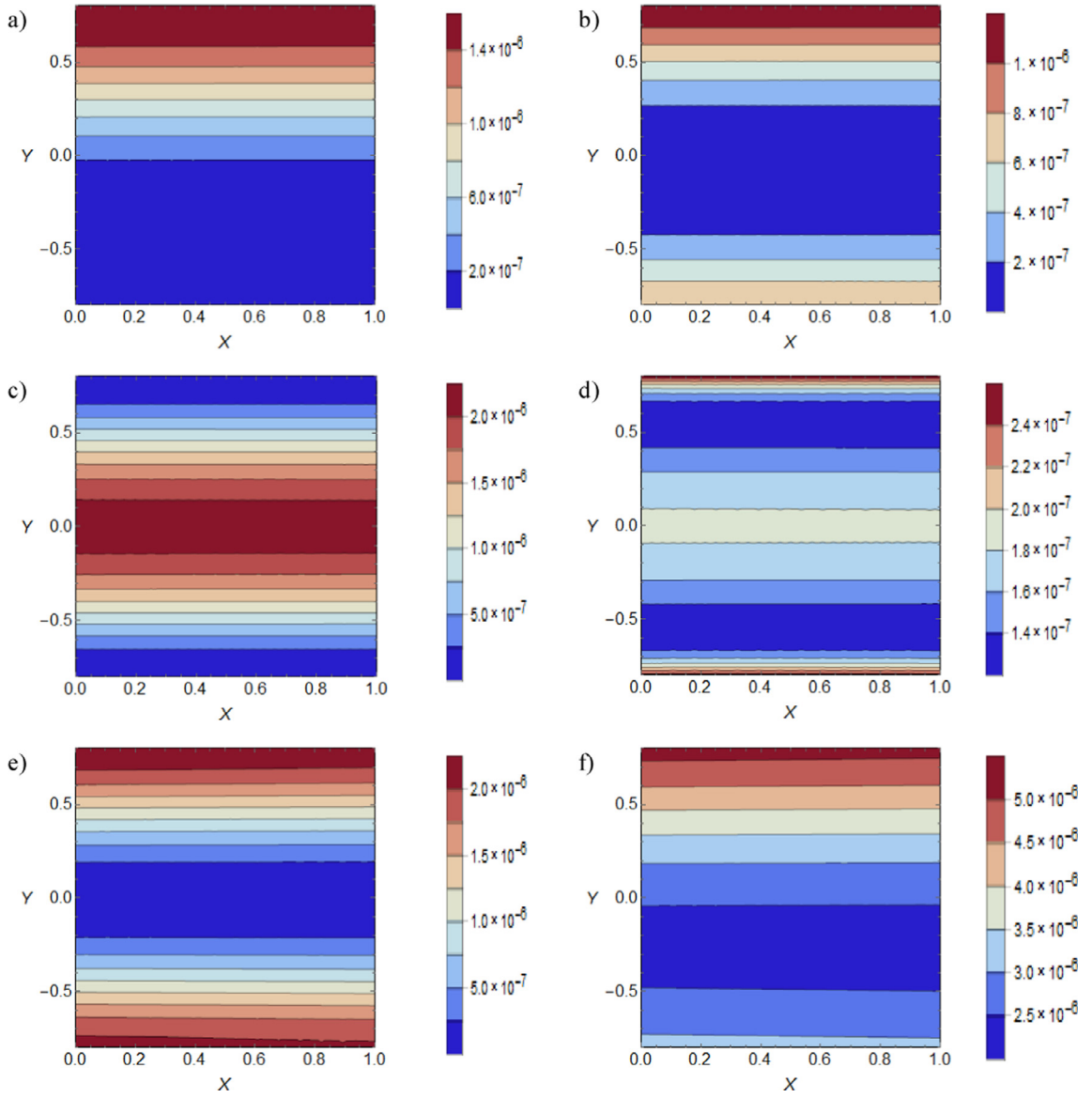

Fig. 12. Entropy contours for Damköhler number, $\gamma = 0.1$ with $Sr = 0$ for; (a) $N_{s,ht}$, (b) $N_{nf,ht}$, (c) N_{int}, (d) N_{FF}, (e) N_{DI} and (f) N_{pm}.

$$D_2 = Br' D_1^2 S^2 \tag{B1b}$$

$$D_3 = \frac{D_1}{Y_1} - D_2 \cosh(SY_1) \tag{B1c}$$

$$D_4 = -\frac{D_1}{Y_1}\cosh(SY_1). \tag{B1d}$$

$$E_1 = \frac{2QY_1 - k_{e2}\theta_{w2}}{k_{e2}}, \quad E_2 = \frac{2Q}{k_{e2}}, \tag{B2a, b}$$

$$E_3 = \frac{BiD_2 - 4D_2S^2}{16kS^4 - 4kS^2\alpha^2}, \quad E_4 = \frac{BiD_3 - D_3S^2}{kS^4 - kS^2\alpha^2}, \tag{B2c, d}$$

$$E_5 = \frac{-[D_4 + 2E_6k + (D_3 + E_4kS^2)\cosh(SY_1) + (D_2 + 4E_3kS^2)\cosh(2SY_1)]\mathrm{sech}(\alpha Y_1)}{k\alpha^2}, \tag{B2e}$$

$$E_6 = \frac{-BiD_4}{2k\alpha^2}, \quad E_7 = \frac{\theta_{w2}}{2Y_1}, \tag{B2f, g}$$

$$E_8 = \frac{1}{2k\alpha^2}[2D_4 + 2E_6k(2 - Y_1^2\alpha^2) + k\alpha^2\theta_{w2} + 2(D_3 + E_4k(S^2 - \alpha^2))\cosh(SY_1) + 2(D_4 + E_3k(4S^2 - \alpha^2))\cosh(2SY_1)], \tag{B2h}$$

$$E_9 = \frac{BiD_2}{16kS^4 - 4kS^2\alpha^2}, \quad E_{10} = \frac{BiD_3}{kS^4 - kS^2\alpha^2}, \tag{B2i, j}$$

$$E_{11} = \frac{-[2E_6 + E_{10}S^2\cosh(SY_1) + 4E_9S^2\cosh(2SY_1)]\mathrm{sech}(\alpha Y_1)}{\alpha^2}, \tag{B2k}$$

$$E_{12} = \frac{1}{2\alpha^2}[4E_6 - 2E_6Y_1^2\alpha^2 + \alpha^2\theta_{w2} + 2E_{10}(S^2 - \alpha^2)\cosh(SY_1) + 2E_9(4S^2 - \alpha^2)\cosh(2SY_1)], \tag{B2l}$$

$$E_{13} = \frac{2(Q-1)Y_1}{k_{e1}}, \quad E_{14} = \frac{2(Q-1)}{k_{e1}} \tag{B2m, n}$$

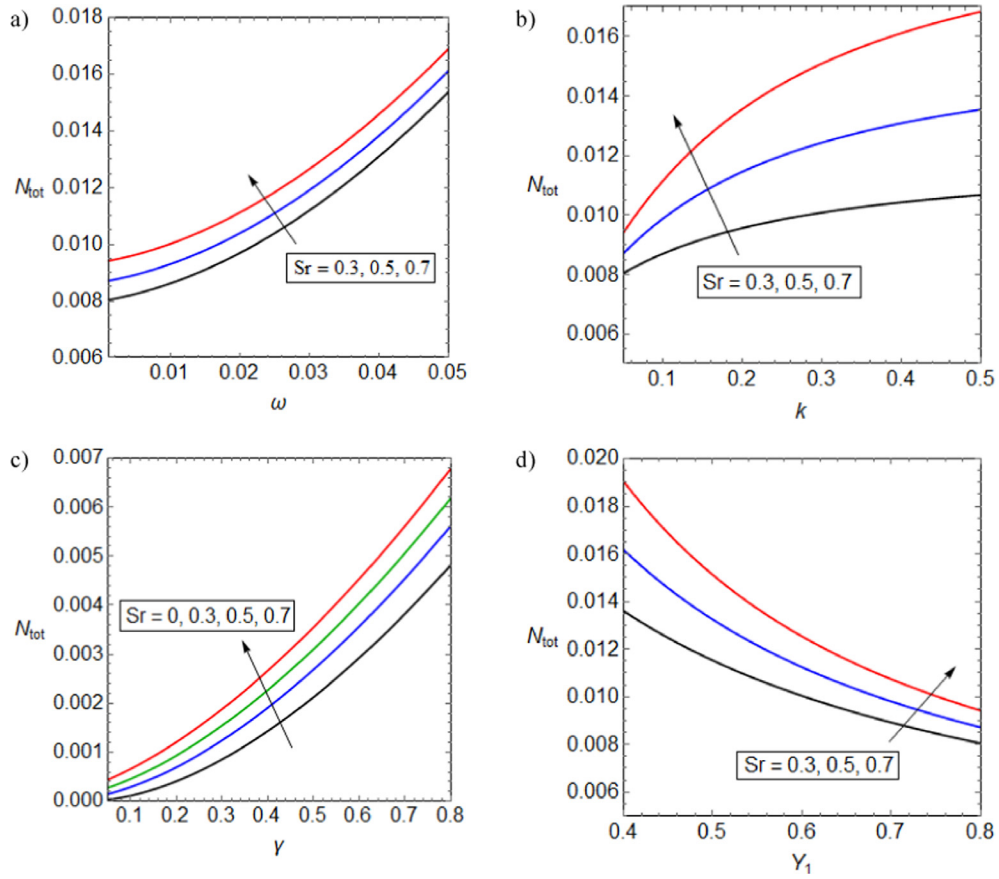

Fig. 13. Total Entropy generation for different values of Soret number, *Sr* against varying (a) dimensionless heat flux, ω (b) thermal conductivity ratio, k (c) Damköhler number, γ and (d) dimensionless thickness of the lower wall, Y_1.

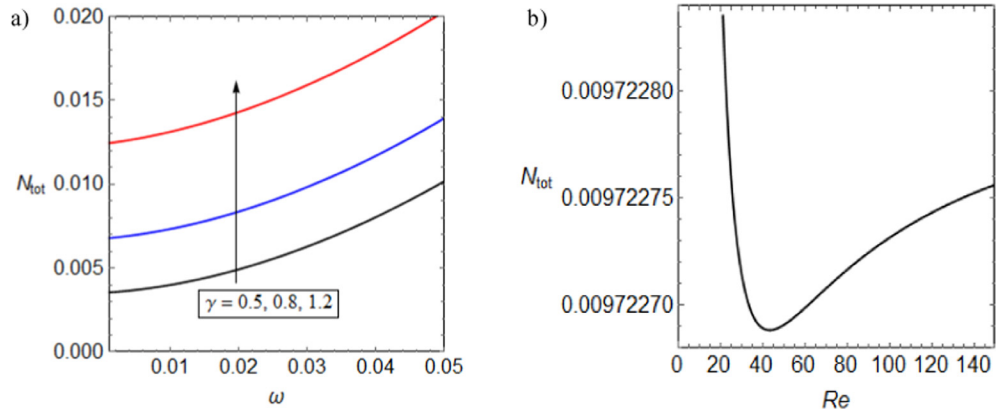

Fig. 14. Total Entropy against (a) dimensionless heat flux, ω and (b) Reynolds number, *Re*.

Since the top wall temperature is not known in advance, it is necessary to find the equation by which it is defined. This may be accomplished by using the dimensionless form of the boundary condition in Eq. (4b), which defines q_2'':

$$\theta_s'(Y_1) + k\theta_{nf}'(Y_1) = 2Q. \tag{B3}$$

Substituting from Eqs. (20b) and (20c) and some algebraic manipulations lead to

$$\theta_{w2} = \frac{Y_1[4QS + 2D_4SY_1 + 2D_3\sinh(SY_1) + D_2\sinh(2SY_1)]}{S(k+1)} \tag{B4}$$

Appendix C. Validation

To validate the mathematical model developed in Section 2, it is demonstrated here that when the wall thickness tends to zero, the temperature fields reduce to that presented by Ting et al. [32] with no internal heat generation term. To produce a system equivalent to that of Ref. [32], we set $h_1 = h_2$, that is in terms of non-dimensional parameters; $Y_1 = 1$ and also $q_{gen}''' = 0$, which renders $\Omega_{gen} = 0$. The momentum Eqs. (9)-(11) can clearly be seen to reduce to the corresponding equations. Utilising these, Eqs. (15) becomes,

$$\frac{d\bar{T}_{nf}}{dx} = \frac{1}{2\rho_{nf}C_{p,nf}\bar{u}h_2^2}\left[h_2 q_1'' + h_2 q_2'' + \frac{2\mu_{eff}S^3\bar{u}^2\cosh(S)}{S\cosh(S)-\sinh(S)}\right] = \Omega_T \tag{C1}$$

This is the same as the axial thermal gradient found by Ting et al. [32] with no heat generation term. Next, the radial thermal equations can be determined from Eqs. (17b) and (17c) using the given conditions to yield the coupled equations:

$$k\theta_{nf}'' + Bi(\theta_s - \theta_{nf}) + D_2'\cosh(2SY) + D_3'\cosh(SY) + D_4' = 0, \quad -1 \leqslant Y < 1 \tag{C2a}$$

$$\theta_s'' - Bi(\theta_s - \theta_{nf}) = 0, \quad -1 \leqslant Y < 1 \tag{C2b}$$

where the modified coefficients (which are shown by use of a prime) are:

$$D_1' = \frac{S}{S\cosh(S)-\sinh(S)} \tag{C3a}$$

$$D_2' = Br' D_1'^2 S^2 \tag{C3b}$$

$$D_3' = D_1' - D_2'\cosh(S) \tag{C3c}$$

$$D_4' = -D_1'\cosh(S) \tag{C3d}$$

The coefficients $D_1' - D_4'$ are the same as those calculated by Ting et al. for the coupled thermal equations investigated therein under the previously stated conditions. Thus, it follows that the final nanofluid and porous solid thermal equations, Eqs. (20b) and (20c) may be recast using these conditions to give the following:

$$\theta_{nf}(Y) = E_3'\cosh(2SY) + E_4'\cosh(SY) + E_5'\cosh(\alpha Y) + E_6' Y^2 + E_7' Y + E_8' \quad -1 \leqslant Y < 1 \tag{C4a}$$

$$\theta_s(Y) = E_9'\cosh(2SY) + E_{10}'\cosh(SY) + E_{11}'\cosh(\alpha Y) + E_6' Y^2 + E_7' Y + E_{12}' \quad -1 \leqslant Y < 1 \tag{C4b}$$

where the new coefficients are defined as:

$$E_3' = \frac{D_2'(4S^2 - Bi)}{4S^2(-4kS^2 + Bik + Bi)}, \quad E_4' = \frac{D_3'(S^2 - Bi)}{S^2(k\alpha^2 - kS^2)}, \tag{C5a, b}$$

$$E_5' = \frac{-[D_4' + 2E_6' k + (D_3' + E_4' kS^2)\cosh(S) + (D_2' + 4E_3' kS^2)\cosh(2S)]\mathrm{sech}(\alpha)}{Bi(k+1)}, \tag{C5c}$$

$$E_6' = \frac{-D_4'}{2(k+1)}, \quad E_7' = \frac{\theta_{w2}'}{2}, \tag{C5d, e}$$

$$E_8' = \frac{1}{2k\alpha^2}[2D_4' + 2E_6' k(2-\alpha^2) + k\alpha^2\theta_{w2}' + 2(D_3' + E_4' k(S^2 - \alpha^2))\cosh(S) + 2(D_4' + E_3' k(4S^2 - \alpha^2))\cosh(2S)], \tag{C5f}$$

$$E_9' = \frac{BiE_3'}{Bi - 4S^2}, \quad E_{10}' = \frac{BiE_4'}{Bi - S^2}, \tag{C5g, h}$$

$$E_{11}' = \frac{-[2E_6' + E_{10}' S^2\cosh(S) + 4E_9' S^2\cosh(2S)]\mathrm{sech}(\alpha)}{\alpha^2}, \tag{C5i}$$

$$E_{12}' = \frac{1}{2\alpha^2}[4E_6' - 2E_6'\alpha^2 + \alpha^2\theta_{w2} + 2E_{10}'(S^2 - \alpha^2)\cosh(S) + 2E_9'(4S^2 - \alpha^2)\cosh(2S)], \tag{C5j}$$

With the appropriate rearranging of terms, these coefficients show that Eqs. (C4a) and (C4b) are analytically identical to the nanofluid and porous solid thermal equations presented in the work by Ting et al. [32].

References

[1] V. Hessel, A. Renken, J.C. Schouten, J.-I. Yoshida (Eds.), Micro Process Engineering, Wiley-VCH Verlag GmbH & Co. KGaA, Weinheim, Germany, 2009, doi:10.1002/9783527631445.

[2] X. Yao, Y. Zhang, L. Du, J. Liu, J. Yao, Review of the applications of microreactors, Renew. Sustain. Energy Rev. 47 (2015) 519–539, https://doi.org/10.1016/j.rser.2015.03.078.

[3] N. Kockmann, Transport Phenomena in Micro Process Engineering, Springer, NY, 2008.

[4] T. Wirth, Microreactors in Organic Chemistry and Catalysis, 2013, 470.

[5] G. Kolb, Review: Microstructured reactors for distributed and renewable production of fuels and electrical energy, Chem. Eng. Process. Process Intensif. 65 (2013) 1–44, https://doi.org/10.1016/j.cep.2012.10.015.

[6] M. Rahimi, B. Aghel, M. Alitabar, A. Sepahvand, H.R. Ghasempour, Optimization of biodiesel production from soybean oil in a microreactor, Energy Convers. Manage. 79 (2014) 599–605, https://doi.org/10.1016/j.enconman.2013.12.065.

[7] H.S. Santana, D.S. Tortola, J.L. Silva, O.P. Taranto, Biodiesel synthesis in micromixer with static elements, Energy Convers. Manage. 141 (2017) 28–39, https://doi.org/10.1016/j.enconman.2016.03.089.

[8] S. Sharada, P.L. Suryawanshi, R. Kumar P., S.P. Gumfekar, T.B. Narsaiah, S.H. Sonawane, Synthesis of palladium nanoparticles using continuous flow microreactor, Colloids Surfaces A Physicochem. Eng. Asp. 498 (2016) 297–304, https://doi.org/10.1016/j.colsurfa.2016.03.068.

[9] N.S. Kaisare, D.G. Vlachos, A review on microcombustion: Fundamentals, devices and applications, Prog. Energy Combust. Sci. 38 (2012) 321–359, https://doi.org/10.1016/j.pecs.2012.01.001.

[10] G. Kolb, V. Hessel, Micro-structured reactors for gas phase reactions, Chem. Eng. J. 98 (2004) 1–38, https://doi.org/10.1016/j.cej.2003.10.005.

[11] R. Guettel, T. Turek, Assessment of micro-structured fixed-bed reactors for highly exothermic gas-phase reactions, Chem. Eng. Sci. 65 (2010) 1644–1654, https://doi.org/10.1016/j.ces.2009.11.002.

[12] G. Hunt, N. Karimi, M. Torabi, Analytical investigation of heat transfer and classical entropy generation in microreactors – the influences of exothermicity and asymmetry, Appl. Therm. Eng. 119 (2017) 403–424, https://doi.org/10.1016/j.applthermaleng.2017.03.057.

[13] M. Torabi, A. Elliott, N.K. Karimi, Thermodynamics analyses of porous microchannels with asymmetric thick walls and exothermicity: an entropic model of micro-reactors, J. Therm. Sci. Eng. Appl. (2017), https://doi.org/10.1115/1.4036802.

[14] M. Torabi, M. Torabi, G.P. Peterson, Entropy generation of double diffusive forced convection in porous channels with thick walls and Soret effect, Entropy 19 (2017) 171, https://doi.org/10.3390/e19040171.

[15] H. Ammar, B. Garnier, A. Ould el Moctar, H. Willaime, F. Monti, H. Peerhossaini, Thermal analysis of chemical reactions in microchannels using highly sensitive thin-film heat-flux microsensor, Chem. Eng. Sci. 94 (2013) 150–155, https://doi.org/10.1016/j.ces.2013.02.055.

[16] R. Sui, N.I. Prasianakis, J. Mantzaras, N. Mallya, J. Theile, D. Lagrange, M. Friess, An experimental and numerical investigation of the combustion and heat transfer characteristics of hydrogen-fueled catalytic microreactors, Chem. Eng. Sci. 141 (2016) 214–230, https://doi.org/10.1016/j.ces.2015.10.034.

[17] S. Schwolow, J.Y. Ko, N. Kockmann, T. Roder, Enhanced heat transfer by exothermic reactions in laminar flow capillary reactors, Chem. Eng. Sci. 141 (2016) 356–362, https://doi.org/10.1016/j.ces.2015.11.022.

[18] E.V. Rebrov, J.C. Schouten, M.H.J.M. de Croon, Single-phase fluid flow distribution and heat transfer in microstructured reactors, Chem. Eng. Sci. 66 (2011) 1374–1393, https://doi.org/10.1016/j.ces.2010.05.044.

[19] R.-Y. Chein, L.-C. Chen, Y.-C. Chen, J.N. Chung, Heat transfer effects on the methanol-steam reforming with partially filled catalyst layers, Int. J. Hydrogen Energy 34 (2009) 5398–5408, https://doi.org/10.1016/j.ijhydene.2009.04.049.

[20] R.-Y. Chein, Y.-C. Chen, J.N. Chung, Thermal resistance effect on methanol-steam reforming performance in micro-scale reformers, Int. J. Hydrogen Energy 37 (2012) 250–262, https://doi.org/10.1016/j.ijhydene.2011.09.070.

[21] R.-Y. Chein, Y.-C. Chen, H.-J. Zhu, J.N. Chung, Numerical simulation of flow disturbance and heat transfer effects on the methanol-steam reforming in miniature annulus type reformers, Energy Fuels 26 (2012) 1202–1213, https://doi.org/10.1021/ef201498t.

[22] R. Chein, Y.-C. Chen, J.N. Chung, Axial heat conduction and heat supply effects on methanol-steam reforming performance in micro-scale reformers, Int. J. Heat Mass Transf. 55 (2012) 3029–3042, https://doi.org/10.1016/j.ijheatmasstransfer.2012.02.022.

[23] N. Karimi, D. Agbo, A. Talat Khan, P.L. Younger, On the effects of exothermicity and endothermicity upon the temperature fields in a partially-filled porous channel, Int. J. Therm. Sci. 96 (2015) 128–148, https://doi.org/10.1016/j.ijthermalsci.2015.05.002.

[24] M. Torabi, N. Karimi, K. Zhang, Heat transfer and second law analyses of forced convection in a channel partially filled by porous media and featuring internal heat sources, Energy 93 (2015) 106–127, https://doi.org/10.1016/j.energy.2015.09.010.

[25] M. Torabi, N. Karimi, K. Zhang, G.P. Peterson, Generation of entropy and forced convection of heat in a conduit partially filled with porous media – local thermal non-equilibrium and exothermicity effects, Appl. Therm. Eng. 106 (2016) 518–536, https://doi.org/10.1016/j.applthermaleng.2016.06.036.
[26] C. Dickson, M. Torabi, N. Karimi, First and second law analyses of nanofluid forced convection in a partially-filled porous channel – the effects of local thermal non-equilibrium and internal heat sources, Appl. Therm. Eng. 103 (2016) 459–480, https://doi.org/10.1016/j.applthermaleng.2016.04.095.
[27] K. Hooman, Heat and fluid flow in a rectangular microchannel filled with a porous medium, Int. J. Heat Mass Transf. 51 (2008) 5804–5810, https://doi.org/10.1016/j.ijheatmasstransfer.2008.05.010.
[28] B. Buonomo, O. Manca, G. Lauriat, Forced convection in micro-channels filled with porous media in local thermal non-equilibrium conditions, Int. J. Therm. Sci. 77 (2014) 206–222.
[29] T.W. Ting, Y.M. Hung, N. Guo, Viscous dissipative forced convection in thermal non-equilibrium nanofluid-saturated porous media embedded in microchannels, Int. Commun. Heat Mass Transf. 57 (2014) 309–318, https://doi.org/10.1016/j.icheatmasstransfer.2014.08.018.
[30] T.W. Ting, Y.M. Hung, N. Guo, Field-synergy analysis of viscous dissipative nanofluid flow in microchannels, Int. J. Heat Mass Transf. 73 (2014) 483–491, https://doi.org/10.1016/j.ijheatmasstransfer.2014.02.041.
[31] T.W. Ting, Y.M. Hung, N. Guo, Entropy generation of nanofluid flow with streamwise conduction in microchannels, Energy 64 (2014) 979–990, https://doi.org/10.1016/j.energy.2013.10.064.
[32] T.W. Ting, Y.M. Hung, N. Guo, Entropy generation of viscous dissipative nanofluid convection in asymmetrically heated porous microchannels with solid-phase heat generation, Energy Convers. Manage 105 (2015) 731–745, https://doi.org/10.1016/j.enconman.2015.08.022.
[33] G. Ibáñez, S. Cuevas, Entropy generation minimization of a MHD (magnetohydrodynamic) flow in a microchannel, Energy 35 (2010) 4149–4155, https://doi.org/10.1016/j.energy.2010.06.035.
[34] M. Torabi, G.P. Peterson, Effects of velocity slip and temperature jump on the heat transfer and entropy generation in micro porous channels under magnetic field, Int. J. Heat Mass Transf. 102 (2016) 585–595, https://doi.org/10.1016/j.ijheatmasstransfer.2016.06.080.
[35] A. Elliott, M. Torabi, N. Karimi, S. Cunningham, On the effects of internal heat sources upon forced convection in porous channels with asymmetric thick walls, Int. Commun. Heat Mass Transf. 73 (2016) 100–110, https://doi.org/10.1016/j.icheatmasstransfer.2016.02.016.
[36] N. Verma, D. Mewes, A. Luke, Lattice Boltzmann study of velocity, temperature, and concentration in micro-reactors, Int. J. Heat Mass Transf. 53 (2010) 3175–3185, https://doi.org/10.1016/j.ijheatmasstransfer.2010.03.009.
[37] W.-H. Chen, T.-C. Cheng, C.-I. Hung, Numerical predictions on thermal characteristic and performance of methanol steam reforming with microwave-assisted heating, Int. J. Hydrogen Energy. 36 (2011) 8279–8291, https://doi.org/10.1016/j.ijhydene.2011.04.145.
[38] F. Wang, J. Zhou, G. Wang, Transport characteristic study of methane steam reforming coupling methane catalytic combustion for hydrogen production, Int. J. Hydrogen Energy 37 (2012) 13013–13021, https://doi.org/10.1016/j.ijhydene.2012.05.062.
[39] N. Meynet, A. Bentaib, V. Giovangigli, Impact of oxygen starvation on operation and potential gas-phase ignition of passive auto-catalytic recombiners, Combust. Flame 161 (2014) 2192–2202, https://doi.org/10.1016/j.combustflame.2014.02.001.
[40] M.H. Matin, I. Pop, Forced convection heat and mass transfer flow of a nanofluid through a porous channel with a first order chemical reaction on the wall, Int. Commun. Heat Mass Transf. 46 (2013) 134–141, https://doi.org/10.1016/j.icheatmasstransfer.2013.05.001.
[41] P.S. Reddy, A.J. Chamkha, Soret and Dufour effects on MHD convective flow of Al2O3-water and TiO2-water nanofluids past a stretching sheet in porous media with heat generation/absorption, Adv. Powder Technol. 27 (2016) 1207–1218, https://doi.org/10.1016/j.apt.2016.04.005.
[42] A. Bahloul, N. Boutana, P. Vasseur, Double-diffusive and Soret-induced convection in a shallow horizontal porous layer, J. Fluid Mech. 491 (2003) 325–352, https://doi.org/10.1017/S0022112003005524.
[43] D. Ingham, I. Pop, Transport Phenomena in Porous Media III, 2005.
[44] Y. Wenming, J. Dongyue, C.K.Y. Kenny, Z. Dan, P. Jianfeng, Combustion process and entropy generation in a novel microcombustor with a block insert, Chem. Eng. J. 274 (2015) 231–237, https://doi.org/10.1016/j.cej.2015.04.034.
[45] U. Rana, S. Chakraborty, S.K. Som, Thermodynamics of premixed combustion in a heat recirculating micro combustor, Energy 68 (2014) 510–518, https://doi.org/10.1016/j.energy.2014.02.070.
[46] D. Jiang, W. Yang, K.J. Chua, Entropy generation analysis of H2/air premixed flame in micro-combustors with heat recuperation, Chem. Eng. Sci. 98 (2013) 265–272, https://doi.org/10.1016/j.ces.2013.05.038.
[47] T.W. Ting, Y.M. Hung, N. Guo, Entropy generation of viscous dissipative nanofluid flow in thermal non-equilibrium porous media embedded in microchannels, Int. J. Heat Mass Transf. 81 (2015) 862–877, https://doi.org/10.1016/j.ijheatmasstransfer.2014.11.006.
[48] M. Torabi, C. Dickson, N. Karimi, Theoretical investigation of entropy generation and heat transfer by forced convection of copper–water nanofluid in a porous channel — local thermal non-equilibrium and partial filling effects, Powder Technol. 301 (2016) 234–254, https://doi.org/10.1016/j.powtec.2016.06.017.
[49] M. Torabi, K. Zhang, N. Karimi, G.P. Peterson, Entropy generation in thermal systems with solid structures – a concise review, Int. J. Heat Mass Transf. 97 (2016) 917–931, https://doi.org/10.1016/j.ijheatmasstransfer.2016.03.007.
[50] H. Abbassi, Entropy generation analysis in a uniformly heated microchannel heat sink, Energy. 32 (2007) 1932–1947, https://doi.org/10.1016/j.energy.2007.02.007.
[51] W.M. Deen, Analysis of Transport Phenomena, Oxford University Press, 1998.
[52] H.C. Brinkman, The Viscosity of Concentrated Suspensions and Solutions, J. Chem. Phys. 20 (1952), https://doi.org/10.1063/1.1700493, 571–571.
[53] K. Khanafer, K. Vafai, M. Lightstone, Buoyancy-driven heat transfer enhancement in a two-dimensional enclosure utilizing nanofluids, Int. J. Heat Mass Transf. 46 (2003) 3639–3653, https://doi.org/10.1016/S0017-9310(03)00156-X.